A contact description for continuum beams with deformable arbitrary cross-section

Babak Bozorgmehri[a,b,c,*], Leonid P. Obrezkov[a], Ajay B. Harish[d], Aki Mikkola[a] and Marko K. Matikainen[a]

[a] LUT Mechanical Engineering, School of Energy Systems, LUT University, Lappeenranta, Finland
[b] Department of Mechanical Engineering, KU Leuven, 3001 Heverlee, Belgium
[c] DMMS, Flanders Make @ KU Leuven, Belgium
[d] Department of Mechanical, Aerospace and Civil Engineering, University of Manchester, Manchester, United Kingdom

ARTICLE INFO

Keywords:
Beam-to-beam contact
Arbitrary cross-section
Surface-to-surface
Absolute nodal coordinate formulation
Internal contact

ABSTRACT

This work introduces a surface-to-surface contact description in the context of beam-to-beam contact. The introduced contact description is formulated in the frame work of the absolute nodal coordinate formulation. Leveraging the solid element-like features of the absolute nodal coordinate beam formulation and utilizing an interpolation scheme to parameterize the cross-section geometry, the computationally expensive discretization in beam's thickness directions can be avoided. The developed formulation is general to account for internal and external contact scenarios. Numerical examples illustrate the robustness and applicability of the introduced formulation in contact problems comprising beams with arbitrary cross-sectional geometry and material nonlinearities. The numerical results indicate the effectiveness of the proposed contact solution to problems entailing various contact configurations, such as the presence of coupled large deformation modes within contact, contact between beams with sharp-edges, and a scenario where an arbitrary curve-to-curve contact takes place across beams' surfaces. Accuracy of the contact integrals and the stability of the proposed formulation are also examined, respectively using the contact path and inf-sup tests.

1. Introduction

Numerous places where a highly flexible, beam-like structure plays a crucial role can be found in mechanical and bio-mechanical applications. Belts, ropes and cables are examples of the mechanical applications while slender soft tissues are one example of bio-mechanical applications. In many cases, the high-tensile or twisted cables in working cranes, fibrous tissues and filaments in biological systems interact with each other. The applications mentioned earlier, are characterized by mechanical contact interactions where the geometrically complex contact configurations usually exist between beam-like structures.

Compared with the intensive work that has been performed on solid-based contact formulations [1, 2, 3, 4, 5] as for the distributed contact force evolution in a simulation, the research contributions to the beam-to-beam surface contact formulation regarding the distribution of contact force in beam-to-beam contact have marginally been developed.

In the beam-to-beam contact, depending on the contact configurations and the underlying beam finite element formulation used, an adequate contact solution procedure should be considered particularly in the definition of the contact normal vector. To alleviate the shortage of contact points contribution (i.e., non-smoothness through the contact points) in the definition of normal and tangent contact vectors, a Hermitian interpolation for two adjacent beams was introduced in [6]. This smoothing procedure improves the stability of the formulation and the contact stress distribution over a contact region when (frictional) sliding takes place [7]. Durville introduced an intermediate geometry where a proximity zone can be defined to detect the contact point candidates in application of fibrous

*Corresponding author
babak.bozorgmehri@kuleuven.be (B. Bozorgmehri)
ORCID(s): 0000-0003-2400-6768 (B. Bozorgmehri)

material in [8]. Thereafter, Durville et al. [9] captured the initial configuration and the possible interpenetration between the bundles of initially contacting interlock fibrous materials. With reference to the distribution of contact force, Meier et al. [10] developed a variant of line-to-line contact formulation with a particular emphasis on integration interval segmentation in the vicinity of strong discontinuity at the end-points of the contacting beams. The limitations of the line-to-line formulation [10] were discussed in [11] and a new formulation was proposed to integrate the advantages of both the point-to-point and line-to-line formulations by introducing a transition procedure between the mentioned formulations. Nevertheless, in Meier et al.'s contributions, the so-called all-angle beam contact model [11] was implemented with a rod-like variant of the Kirchhoff beam theory [12] which ignores cross-section deformation. With the formulations above, the master-and-slave definition needs to be accounted for in the definition of the contact normal vector. One of the drawbacks of such a distinction between the master and slave contact entities is that when using a single-pass algorithm, only the slave nodes / points are checked for interpenetration but not the master points. This can lead to an unchecked interpenetration of the master points. In addition, the weak form of contact energy is biasedly integrated over the slave surface [13]. Although some algorithms make use of a double-pass to preclude this, the double-pass based algorithms are prone to be computationally prohibitive, i.e., locking due to over-constraint at contact points. This was illustrated in [14] in the case of solid elements. This flaw was treated by unbiasedly integrating the weak form of contact energy in [13]. Therein, interchanging of the master-slave roles does not influence the results. Recently, Gay Neto [15, 16] proposed a master-to-master approach in which no distinction is made in a pair of contacting entities (surface / line /point) to be master or slave. Instead, both entities in a contact pair are assumed to be master.

One of the well-established and pioneer beam-to-beam contact formulations was proposed in [17], which is also known as the seminal master-to-master contact description and laid the foundation for further contributions to this context [18, 19, 15, 20].

The continuously defined contact force over a contact interface becomes crucial when beams with deformable cross-sections come into contact. Regardless of the initial contact type, i.e., point-to-point, line-to-line or surface-to-surface, the contact region may evolve from a point to a line or from a line to a surface contact. In the context of beam-to-beam contact, a class of the master surface to master surface formulation was introduced by Gay Neto et al. [18] that allows for the interpolation of the surface of contacting beam elements using a set of convective coordinates composed of the beam element's degrees-of-freedom. The formulation is based on the seminal master-to-master point-wise contact interaction introduced in [17] that laid the foundation for further contributions to this context [21, 19, 15, 20]. The solutions to the local contact problems in these master-master approaches were prone to divergence [20, 16]. To remedy this, recently in [16], an optimization procedure based on the Hessian of the closest projected point problems was replaced with Newton's iterative scheme to achieve a converged solution. In all these works, the contact action-reaction is assumed to be an approximation of the actual distributed force on material points within the contacting surfaces. Alternatively, it would be preferable to apply the actual distributed action-reaction through the nodal degrees-of-freedom over the contacting beams' surface. This is useful when cross-section deformable beams with non-typical cross-sectional shapes come into contact (i.e., large contact region in the initial configuration), and when contacting beams are parallel or wrapping around each other. The latter situation was recently handled in [22] by integrating the weak form of contact energy along the slave beam centre line curve (but not surface) in the case of beams with elliptical, shear deformable (but rigid) cross-section. Distribution of contact action-reaction force is also crucial when a contact region within beams with deformable cross-sections becomes larger during simulation or evolves from a line to a surface. For example, due to highly deformable cross-sections in contact between beams with higher-order interpolations in their basis polynomials, the contact action has to be distributed over a pair of contacting surfaces via the beam element degrees-of-freedom within the simulation. It is also possible that a surface-to-surface interaction degenerates into a surface to line (e.g., surface to sharp edges) or into surface to point. These scenarios were discussed in [15], where the local contact problem in the point-wise surface-to-surface description is degenerated into a surface- to-line or surface-to-point to circumvent singularity problems.

Many of the finite element methods have been formulated using a one-dimensional beam theory, the so-called Simo-Reissner beam [23]. This theory, is the basis of many beam formulations in the framework of the fully nonlinear geometrically exact beams (GEB) with shear-deformable cross-section [24, 25, 26], and with shear-free cross-section [12, 27, 28]. Another fully geometrically nonlinear beam formulation is described in the framework of the absolute nodal coordinate formulation (ANCF) [29, 30] which assumes that the beam's cross-section is deformable. In the ANCF, the kinematics of flexible spatial bodies, such as beams or shells, can be described using polynomial based spatial element shape functions and the vector of nodal coordinates of an element. Absolute positions and components of the deformation gradient that are derived either with respect to the bi-normalized or physical coordinates, are used as nodal degrees-of-freedom in an ANCF element [29]. Description of an ANCF element's strain energy in the spatial elasticity is a crucial distinction between ANCF and the GEB formulation, which relies on the one-dimensional elastic line theory. Thereby, the incorporation of the nonlinear material models into the ANCF becomes more feasible [31, 32]. Whether the strain energy of an ANCF element is derived in terms of the components of the generalized spatial strains [33], or with respect to the components of the deformation gradient [34, 35], the ANCF exhibits the features that are typically recognized in the solid element types. Most recently, a continuous beam-type model is developed in [36] with the inclusion of the solid-like features of material nonlinearity and also the geometry nonlinearity in the study of the flexibility of arching masonry walls subjected to out-of-plane loads. Within the finite element analysis with ANCF elements, there have been a few attempts made to go beyond the standard cross-sections, such as rectangular and circular forms. Nonetheless, they intend to capture only a local deviation from common cases [37, 38] and therefore, they are not suitable for addressing a sophisticated cross-sectional areas. Recently in [39], a computational model based on the ANCF was introduced to describe the pre-twisted Achilles sub-tendons as beam-like structures with arbitrary cross-sectional shapes using nearly incompressible material models to approximate the pre-twisted sub-tendons under tensile loads. The usability and limitations of some higher- and lower-order ANCF beams under torsional and bi-moment loads has lately been studied in [40].

The approach used in Gay Neto et al.'s works [18, 20, 16, 41] to interpolate the contacting surfaces, can conceptually be compared with the spatial shape function to interpolate the lower- or higher-order elements in the case of ANCF beams or plates [42, 43, 44]. For instance, Yu et al. used the spatial shape function interpolation to describe a point-to-point contact between a general rigid surface and a beam's surface in the two-dimensional implementation of an ANCF beam [45]. Recently, in [46] the efficiency of a higher-order ANCF element in terms of the numerical integration on the contact interface was shown with the line-to-line formulation. Taking advantage of the ANCF's spatial shape functions, narrow-phase, local contact detection scheme was implemented to identify the contact points/segments following a global contact search using an oriented bounding box algorithm [47]. An analogy for the treatment of the local contact detection between rob fibres using Lagrangian shape functions to interpolate a contact surface can be found in [48]. The same approach of the local contact search is adopted and extended for the three-dimensional arbitrary shape cross-section in this study.

The primary difference between the line-to-line and surface-to-surface beam contact descriptions is that the former in not applicable to the general description of contact boundaries on the beam's surfaces. The surface-to-surface contact formulation tackles the line-to-line formulation limitations and can help properly impose the contact constraint in general beam contact problems such as the twisting of beams with complicated, highly deformable cross-sections, where the initial contact line (or small region) would evolve to a surface in the deformed configuration. The developed surface-to-surface formulation introduced in this work achieves a converged solution with a reasonable number of discretization, which will be discussed in detail in Section 5. On account of this, an approach is used to approximate an arbitrary-shape cross-section using a numerical integration scheme based on Green's integral formula. This approach is used in this paper as a prerequisite for adapting the employed ANCF beam formulation, to include the contact scenarios in beams with anisotropic, non-typical cross-section shapes undergoing the coupled deformation modes. The proposed cross-section interpolation scheme using the arbitrary splines is utilized in this work to perform the following tasks:

1. the computation of an ANCF beam element internal forces using Gaussian integration scheme across the cross-section with an arbitrary shape
2. the establishment of a contact surface candidate on contacting beams using the Gauss points that are already utilized to interpolate the arbitrary cross-section.

The novelties in connection with the introduced surface-to-surface contact formulation are succinctly stated in the following order:

- A surface-to-surface contact formulation by parameterization (segmentation) of the contacting surfaces, including cross-section boundaries (locally interpolated cross-sections using the selected splines) is proposed.
- The kinematic constituents in the weak form of contact energy are simultaneously integrated across the slave and master beams along two distinct patches.
- With the proposed surface-to-surface contact formulation, as well as the external beam-to-beam contact configuration, the internal surface contact, i.e. contact in interconnected beams, can be formulated.
- The developed contact formulation is able to model the contact scenarios within which a point-wise or a line-to-line contact evolves to a surface-to-surface contact situation and vice versa. In this way, the transition schemes between the contact formulations such as those proposed in [11, 47] are deemed unnecessary.

2. Continuum-based beam finite element

2.1. Beam kinematics

This study employs a spatial three-node beam element based the absolute nodal coordinate formulation (ANCF). In this element, the nodes are located at the ends and in the middle of the beam longitudinal axis [34]. The beam local coordinate system is denoted $\boldsymbol{x} = \{x, y, z\}$, where x is along the beam's axis in the longitudinal direction, and y and z denote the transverse directions. Each node has nine degrees-of-freedom: the three components of position vector $\boldsymbol{r}$ and the three components of the transverse position vector gradients $\boldsymbol{r}_{,y}$ and $\boldsymbol{r}_{,z}$. Accordingly, the vector of the nodal coordinates can be written as:

$$\boldsymbol{q}_I = \left[\boldsymbol{r}^{(I)\mathrm{T}} \;\; \boldsymbol{r}_{,y}^{(I)\mathrm{T}} \;\; \boldsymbol{r}_{,z}^{(I)\mathrm{T}}\right]^T \quad \text{with} \quad I = 1, 2, 3, \tag{1}$$

where $\boldsymbol{r}_{,y}$ is the position vector derivative $\frac{\partial \boldsymbol{r}}{\partial y}$ with respect to y and $\boldsymbol{r}_{,z}$ is $\frac{\partial \boldsymbol{r}}{\partial z}$ in the z direction. The following shape functions (see [34, 49] for details)

$$N_1(\boldsymbol{\xi}) = \frac{1}{2}\left(\xi^2 - \xi\right), \quad N_2(\boldsymbol{\xi}), = \frac{1}{4}\ell_y \eta\left(\xi^2 - \xi\right), \quad N_3(\boldsymbol{\xi}) = \frac{1}{4}\ell_z \zeta\left(\xi^2 - \xi\right), \tag{2a}$$

$$N_4(\boldsymbol{\xi}) = \left(\xi - 1\right)\left(\xi + 1\right), \quad N_5(\boldsymbol{\xi}) = -\frac{1}{2}\ell_y \eta\left(\xi - 1\right)\left(\xi + 1\right), \quad N_6(\boldsymbol{\xi}) = -\frac{1}{2}\ell_z \zeta\left(\xi - 1\right)\left(\xi + 1\right), \tag{2b}$$

$$N_7(\boldsymbol{\xi}) = \frac{1}{2}\xi\left(\xi + 1\right), \quad N_8(\boldsymbol{\xi}) = \frac{1}{4}\ell_y \eta \xi\left(\xi + 1\right) \text{ and } N_9(\boldsymbol{\xi}) = \frac{1}{4}\ell_z \zeta \xi\left(\xi + 1\right) \tag{2c}$$

are defined for the beam element in the bi-normalised local coordinate $\boldsymbol{\xi} = \{\xi, \eta, \zeta\}$ in which the non-dimensional quantities are defined as follows:

$$\xi = \frac{x}{\ell_x}, \;\; \eta = \frac{y}{\ell_y}, \;\; \zeta = \frac{z}{\ell_z}, \tag{3}$$

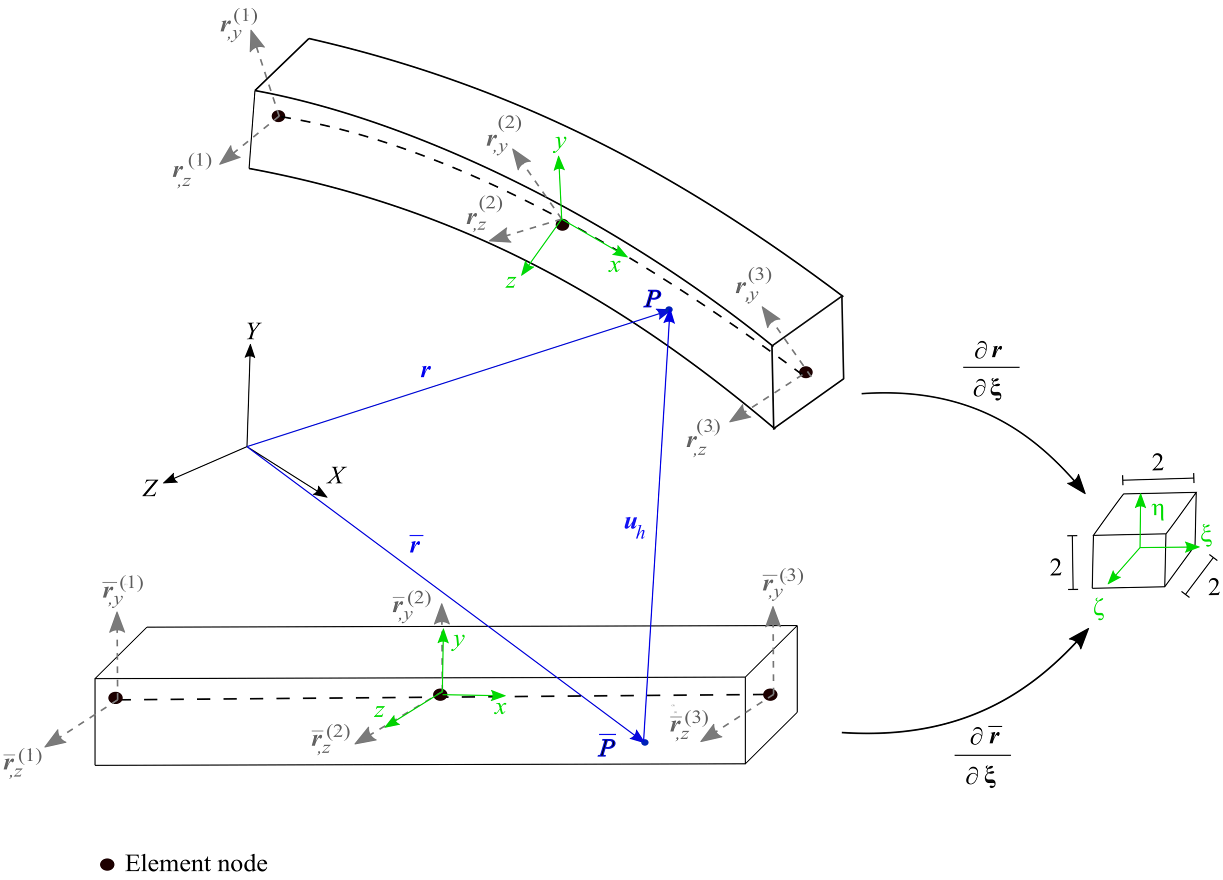

Figure 1: Schematic beam kinematics defined in the reference and deformed configurations with the illustration of the transformation between the bi-normalized and the local elemental coordinates [32].

where ℓ_x is the length, ℓ_y is the height and ℓ_z is the width of a beam element in the undeformed configuration. In the ANCF, the position vector of an arbitrary particle $\boldsymbol{P}$, shown in Figure 1, within an element with respect to the global coordinates system denoted $\boldsymbol{X} = \{X, Y, Z\}$ at time t is

$$\boldsymbol{r}(\xi, t) = \mathbf{N}(\xi)\, \boldsymbol{q}(t) = \bar{\boldsymbol{r}}(\xi, t_0) + \boldsymbol{u}_h(\xi, t), \tag{4}$$

where

$$\boldsymbol{u}_h(\xi, t) = \mathbf{N}(\xi)\, \boldsymbol{u}, \tag{5}$$

is the 3×1 displacement field carrying the particle $\bar{P}$ from its initial position to the current position P and $\boldsymbol{u} = \boldsymbol{q} - \boldsymbol{q}_0$ is a vector of nodal displacements in terms of a beam element's degrees-of-freedom in which $\boldsymbol{q}_0$ and $\boldsymbol{q}$ are the initial and current vector of nodal coordinates, $\bar{\boldsymbol{r}}$ is the initial position of an arbitrary point on a beam element at $t_0 = 0$, and

$$\mathbf{N}(\xi) = \begin{bmatrix} \mathbf{I}N_1 & \mathbf{I}N_2 & \cdots & \mathbf{I}N_9 \end{bmatrix} \tag{6}$$

is the matrix of element shape functions with dimension of 27×3 and $\mathbf{I}$ is the 3×3 identity matrix.

2.2. Weak form of energy equilibrium

In the absolute nodal coordinate formulation when assuming a quasi-static equilibrium, weak form can be expressed as follows:

$$\delta\Pi(\boldsymbol{r},\delta\boldsymbol{r}) = \underbrace{-\int_V \mathbf{S} : \delta\mathbf{E}\mathrm{d}V}_{\delta\Pi_{\mathrm{int}}} + \underbrace{\int_V \boldsymbol{b}^T\delta\boldsymbol{r}\mathrm{d}V + \int_{\partial V}\boldsymbol{p}_a^T\delta\boldsymbol{r}\mathrm{d}\partial V}_{\delta\Pi_{\mathrm{ext}}} + \delta\Pi_{\mathrm{con}} = 0, \tag{7}$$

where $\mathbf{S}$ is the second Piola-Kirchhoff stress tensor, $\mathbf{E}$ is the Green-Lagrange strain tensor, " : " denotes the double dot product, $\boldsymbol{b}$ is the body force vector, which is $\boldsymbol{b} = \rho\boldsymbol{g}$, where $\boldsymbol{g}$ is the field of gravity, $\boldsymbol{p}_a$ is the surface force vector, V denotes integration over an element's volume and ∂V indicates a surface portion belonging to the volume V. In Eq. (7), $\delta\Pi_{\mathrm{int}}$ is the variation in strain energy of the element, $\delta\Pi_{\mathrm{ext}}$ is the variation in work done by externally applied forces, and $\delta\Pi_{\mathrm{con}}$ relates to the variational work done to enforce contact constraint.

The internal force $\boldsymbol{f}_{\mathrm{int}}$ can be derived from the variation of strain energy $\delta\Pi_{\mathrm{int}}$ as follows:

$$\delta\Pi_{\mathrm{int}} = \int_V \mathbf{S} : \frac{\partial\mathbf{E}}{\partial\boldsymbol{u}}\mathrm{d}V\delta\boldsymbol{u} = \boldsymbol{f}_{\mathrm{int}}\delta\boldsymbol{u}. \tag{8}$$

The weak form of strain energy stored in an ANCF element (8) can be written in terms of the split stress tensors $\mathbf{S}_0$ and $\mathbf{S}_v$ ($\mathbf{S} = \mathbf{S}_0 + \mathbf{S}_v$) in the following form

$$\delta\Pi_{\mathrm{int}} = \int_V \left(\mathbf{S}_0 : \frac{\partial\mathbf{E}}{\partial\boldsymbol{u}} + \mathbf{S}_v : \frac{\partial\mathbf{E}}{\partial\boldsymbol{u}}\right)\mathrm{d}V\delta\boldsymbol{u} = \boldsymbol{f}_{0,\mathrm{int}}\delta\boldsymbol{u} + \boldsymbol{f}_{v,\mathrm{int}}\delta\boldsymbol{u}, \tag{9}$$

where $\mathbf{S}_v$ and $\mathbf{S}_0$ are the Piola-Kirchhoff stress tensor parts, respectively excluding and including the Poisson ratio to handle the Poisson (locking) phenomenon, and $\boldsymbol{f}_{0,\mathrm{int}}$ and $\boldsymbol{f}_{v,\mathrm{int}}$ are the corresponding vector of internal forces components [34].

The external force $\boldsymbol{f}_{\mathrm{ext}}$ can be obtained using the variation of energy $\delta\Pi_{\mathrm{ext}}$ as

$$\delta\Pi_{\mathrm{ext}} = \int_V \boldsymbol{b}^T\delta\boldsymbol{r}\,\mathrm{d}V + \int_{\partial V}\boldsymbol{p}_a^T\delta\boldsymbol{r}\mathrm{d}\partial V = \int_V \boldsymbol{b}^T\mathbf{N}\,\mathrm{d}V\delta\boldsymbol{u} + \int_{\partial V}\boldsymbol{p}_a^T\mathbf{N}\mathrm{d}\partial V\delta\boldsymbol{u} = \boldsymbol{f}_{\mathrm{ext}}\delta\boldsymbol{u}. \tag{10}$$

The variation of energy $\delta\Pi_{\mathrm{con}}$ is contributed by contact force and can be written as

$$\delta\Pi_{\mathrm{con}} = \boldsymbol{f}_{\mathrm{con}}\delta\boldsymbol{u}, \tag{11}$$

where $\boldsymbol{f}_{\mathrm{con}}$ represents the contact force, which will be explained in Section 4.

Remark 1. *The variation of strain energy (8) is integrated to derive the vector of element elastic forces according to the developed scheme to define a cross-section geometry, that will be introduced in Section 3. It is derived analogous to the approach for description of the internal forces presented in [34].*

This study employes two widely used hyperelastic material models, the Saint Venant-Kirchhoff and the Neo-Hookean material models. For more details about the Saint Venant-Kirchhoff employed in this paper one can refer to [50] and references therein. More information on the nearly incompressible material model employed here are available for example in [51, 52].

2.2.1. Equations of equilibrium

Substituting Eqs. (8) and (10) into Eq. (7), the weak form of the equations of equilibrium can be expressed as follows:

$$\boldsymbol{f}_{\mathrm{int}}\delta\boldsymbol{u} - \boldsymbol{f}_{\mathrm{ext}}\delta\boldsymbol{u} + \boldsymbol{f}_{\mathrm{con}}\delta\boldsymbol{u} = 0. \tag{12}$$

The spatially discretized version of the variational system of equations in Eq. (12) after assembling the elemental quantities is read in the following form:

$$\boldsymbol{R}^e(\boldsymbol{U}) = -\boldsymbol{F}_{\text{ext}}(\boldsymbol{U}) + \boldsymbol{F}_{\text{int}}(\boldsymbol{U}) + \boldsymbol{F}_{\text{con}}(\boldsymbol{U}), \tag{13}$$

where $\boldsymbol{R}^e(\boldsymbol{U})$ is the vector of residual forces, $\boldsymbol{U}$ is the assembled global displacement vector, $\boldsymbol{F}_{\text{ext}}$, $\boldsymbol{F}_{\text{int}}$, and $\boldsymbol{F}_{\text{con}}$ are the assembled vector of external, internal and contact forces, respectively. Solving Eq. (13) all over the place of application requires the Newton's iteration scheme. One can derive the tangent stiffness matrix of system at the $\boldsymbol{P}^{th}$ iteration by taking Jacobian of the vector of residuals $\boldsymbol{R}^e$ using the following finite difference procedure

$$\mathbf{K}_p^{t(m)} = \frac{\partial \boldsymbol{R}_p^e}{\partial \boldsymbol{U}_p} \approx \sum_{m=1}^{n} \frac{\boldsymbol{R}_p^e\big(\boldsymbol{U}_p + h\hat{\boldsymbol{I}}^{(m)}\big) - \boldsymbol{R}_p^e\big(\boldsymbol{U}_p - h\hat{\boldsymbol{I}}^{(m)}\big)}{2h}, \tag{14}$$

where $\hat{\boldsymbol{I}}^{(m)}$ is the identity vector corresponding to the m^{th} degree-of-freedom of the total n degrees-of-freedom of the system, and h is the reasonable infinitesimal step that is assumed to be $h = 2\ell_x\sqrt{\epsilon_F}$, where machine epsilon $\epsilon_F = 2.220446^{-16}$ in this work [53]. At the next iteration, the displacement vector $\boldsymbol{U}_{p+1}$ is given as

$$\boldsymbol{U}_{p+1} = \boldsymbol{U}_p - (\mathbf{K}_p^t)^{-1}\boldsymbol{R}_p^e \tag{15}$$

provided that the convergence criterion

$$\left\|\boldsymbol{R}_p^e\right\| \leq 10^{-5} \tag{16}$$

holds, where $\left\|\boldsymbol{R}_p^e\right\|$ is the norm of the vector of residuals is checked at iteration p by Eq. (16). The stopping criterion value given by (16) was set for all the numerical examples by which converged solutions with a reasonable number of iterations and beam finite element discretizations can be attained [47].

3. Cross-section approximation

The detail approximation of a cross-section is an important task and has a significant influence on the stress distributions [54]. In this section, the approach introduced in [39] is presented for deriving Gaussian integration points based on the Green's integral formula. The advantage of this method lies in its ability to integrate the whole area without splitting it into sub-domains.

- Let us consider an arbitrary closed domain Ω with a piece-wise border line.
- On the border of the domain $\partial\Omega$ there are some points $V_i,\ i = 1, .., \varphi$, such as $\partial\Omega = [V_1, V_2] \cup [V_2, V_3] \cup \ldots \cup [V_\varphi, V_1]$.
- Besides, the lines $[V_i, V_{i+1}]$ have several additional points, such as $V_{i1} = V_i$ and $V_{i2}, \ldots\ V_{im_i} = V_{i+1}$ [55].
- It should be noted that all the points are already in the bi-normalised local coordinate system $\boldsymbol{\xi}$.

see Section 2.1.

Now we pay attention to the i^{th} line only, i.e., $[V_i, V_{i+1}]$ or $[V_{i1}, V_{im_i}]$, and parameterize it in the following way:

$$[\alpha_{ij}, \beta_{ij}] = \left[0, \sum_{j=1}^{m_i-1} \Delta t_{ij}\right], \quad |\ \Delta t_{ij}\ |=|\ V_{ij+1} - V_{ij}\ |,\ j = 1, ..., m_i - 1. \tag{17}$$

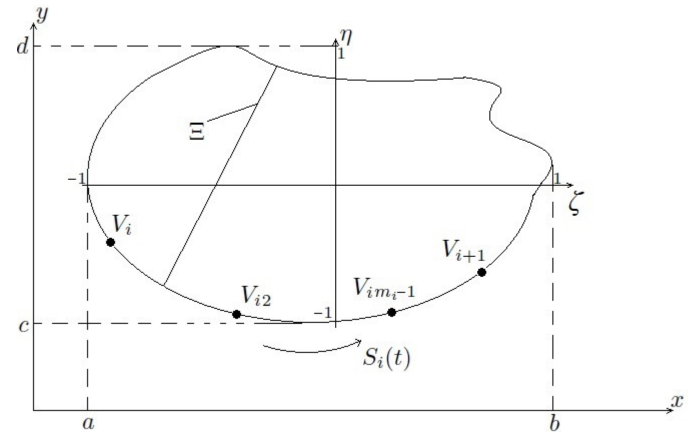

Figure 2: Arbitrary domain Ω in the bi-normalised local coordinate system

Then this $i-$th line is tracked by a spline curve $S_i(t)$ of the degree p_i, where $p_i \leq m_i - 1$ and $S_i(t) = \big(S_{i1}(t), S_{i2}(t)\big)$, see Figure 2. Additionally, we need to define an arbitrary straight line Ξ:

$$\Omega \subseteq \mathbb{R}^2 = [a, b] \times [c, d], \Xi(\eta) \in [a, b], \eta \in [c, d].$$

The choice of Ξ does not have any influence on the results, however, it is necessary for further calculations, because the nodes and weights will be obtained relative to this line [55]. Then, the cubature formula over the domain Ω with the polynomial exactness degree $2n - 1$ takes the following form:

$$I_{2n-1}(f) = \sum_{\lambda \in \Lambda_{2n-1}} w_\lambda f(\eta_\lambda, \zeta_\lambda), \tag{18}$$

where λ is 4-index and is given as follows:

$$\Lambda_{2n-1} = \{\lambda = (i, j, k, h) \,:\, 1 \leqslant i \leqslant \varphi, 1 \leqslant j \leqslant m_i - 11 \leqslant k \leqslant n_i, 1 \leqslant h \leqslant n\} \tag{19}$$

and η_λ and ζ_λ w_λ, are respectively given as follows:

$$\eta_\lambda = \frac{S_{i1}(q_{ijk}) - \Xi}{2} \tau_h^n + \frac{S_{i1}(q_{ijk}) + \Xi}{2}, \tag{20a}$$

$$\zeta_\lambda = S_{i2}(q_{ijk}) \tag{20b}$$

and

$$w_\lambda = \frac{\Delta t_{ij}}{4} \omega_k^{n_i} \omega_h^n (S_{i1}(q_{ijk}) - \Xi) \frac{\mathrm{d}S_{i2}(t)}{\mathrm{d}t} \,|_{t=q_{ijk}}, \tag{20c}$$

in which

$$q_{ijk} = \frac{\Delta t_{ij}}{2} \tau_k^{n_i} + \frac{t_{ij+1} + t_{ij}}{2}, \; \Delta t_{ij} = t_{ij+1} - t_{ij}, \quad \text{with } n_i = \begin{cases} np_i + p_i/2, \; p_i \text{ is even,} \\ np_i + (p_i + 1)/2, \; p_i \text{ is odd.} \end{cases} \tag{21}$$

Only $\tau_k^{n_i}$ and $\omega_k^{n_i}$ need to be defined. They are, respectively, the nodes and weights of the Gauss–Legendre quadrature formula of the exactness degree $2n_i - 1$ on $[-1, 1]$.

As it was anticipated with Remark 1 in Section 2.2, the variation of strain energy (8) is to be integrated within the parametrized domain explained in this section and represented by (18). So in the bi-normalised frame $\boldsymbol{\xi}$, the vector of element elastic forces is obtained by adding the following corresponding Gauss integrals to split the strain energy parts containing $\mathbf{S}_0$ and $\mathbf{S}_v$:

$$\int_V \boldsymbol{f}_{\text{int}}(\xi,\eta,\zeta)\,\mathrm{d}\xi\mathrm{d}\eta\,\mathrm{d}\zeta = \det\left(\frac{\partial\bar{\boldsymbol{r}}}{\partial\xi}\right)\sum_{j=1}^{n_G}\sum_{\lambda\in\Lambda} w_\lambda w_j \boldsymbol{f}_{0,\text{int}}(\xi_j,\eta_\lambda\,\zeta_\lambda) + \det\left(\frac{\partial\bar{\boldsymbol{r}}(1)}{\partial\xi}\right)\sum_{j=1}^{n_G} w_j \boldsymbol{f}_{v,\text{int}}(\xi_j), \tag{22}$$

where n_G and w_j are the number and weight of Gauss points in the longitudinal direction, respectively.

4. Beam-to-beam contact formulations

In this section, a new beam-to-beam contact formulation is introduced. The developed formulation has been inspired by the line-to-line contact procedure in [10] and subsequently, the line-to-line formulation recently developed in the frame work of two-dimensional and three-dimensional ANCF, respectively in [47] and [46]. The line-to-line formulation is first reviewed in Section 4.1 and then a beam surface-to-surface contact formulation is introduced in Section 4.2. The surface-to-surface contact formulation is particularly designed to describe contact in beams with arbitrary non-typical cross-section and in the case of internal contact.

4.1. Line-to-line contact formulation

The unilateral minimum problem for two contacting beams is expressed in terms of closest distance field between the two contacting beams. The closest vector field on beam B (master) $\boldsymbol{r}^B(\xi_c^B)$ corresponding to the position field that belongs to beam A (slave) $\boldsymbol{r}^A(\xi^A)$ is obtained by solving the following minimal distance problem

$$d\left(\xi^A,\xi_c^B(\xi^A)\right) := \min_{\xi^B} d(\xi^A,\xi^B) = \left\|\boldsymbol{r}^B(\xi_c^B) - \boldsymbol{r}^A(\xi^A)\right\|, \tag{23}$$

where subscript $_c$ denotes the closest projected point on the master element for a given slave point, and hereafter it denotes projection of contact entity evaluated at the unilateral closest points. In the line-to-line contact, the unique solution to minimum distance problem (23) leads to one orthogonality condition in which the task is seeking for unknown $\xi_c^B(\xi^A)$, which is the master closest point corresponding to the slave point in terms of the slave coordinate field parameter ξ^A. Assuming contact takes place along a patch between the upper beam (master) at $\eta_c^B = -1$, and the lower beam (slave) at $\eta_c^A = 1$ in the current configuration [56], the closest projection problem

$$h_1(\xi^A,\xi^B) = \left(\boldsymbol{r}^A(\xi^A) - \boldsymbol{r}^B(\xi^B)\right)^T \boldsymbol{r}^B_{,\xi}(\xi^B) \quad \text{with} \;\; h_1(\xi^A,\xi_c^B) = 0 \tag{24}$$

has to be solved; where $\boldsymbol{r}^B_{,\xi}(\xi^B)$ is the derivation of the position vector beam $\boldsymbol{B}$ with respect to local coordinate ξ.

The gap function field $g\left(\xi^A,\xi^B(\xi^A)\right)$ is defined to express the non-penetration condition

$$g\left(\xi^A,\xi^B(\xi^A)\right) = d\left(\xi^A,\xi_c^B(\xi^A)\right) = \left\|\boldsymbol{r}^A_{\eta,\zeta=0} - \boldsymbol{r}^B_{\eta,\zeta=0}\right\| - \left(\left\|\boldsymbol{r}^A - \boldsymbol{r}^A_{c,\eta,\zeta=0}\right\| + \left\|\boldsymbol{r}^B_c - \boldsymbol{r}^B_{c,\eta,\zeta=0}\right\|\right) \;\text{with}\; g\left(\xi^A,\xi^B(\xi^A)\right) \geq 0, \tag{25a}$$

where position field $\boldsymbol{r}^A_{\eta,\zeta=0}$ results from the closest projection of master beam end-point $\boldsymbol{r}^B$ on the slave beam centre line, and $\boldsymbol{r}^B_{\eta,\zeta=0}$ is the vector field resulting from projecting back the slave point abscissa on the closest master element according to Eq. (24). This latter projection task is carried out after the segmentation that will be illustrated in detail in Section 4.1.2.

4.1.1. Enforcement of contact constraint

The gap function field $g\left(\xi^A,\xi^B(\xi^A)\right)$ in terms of the slave beam local parameter ξ^A is defined to express the non-penetration condition

$$g\left(\xi^A,\xi^B(\xi^A)\right) = d(\xi^A,\xi_c^B) \;\text{ with }\; g\left(\xi^A,\xi^B(\xi^A)\right) \geq 0. \tag{26}$$

Accordingly, the variation of contact energy contribution to the equation of equilibrium (7) can be expressed as follows:

$$\delta\Pi_{\text{con}} = p_n \int_{\Omega_c} g\big(\xi^A, \xi^B(\xi^A)\big)\delta g\big(\xi^A, \xi^B(\xi^A)\big)\,\mathrm{d}\Omega_c, \tag{27}$$

where:

$$\delta g(\xi^A, \xi^B(\xi^A)) = \big(\delta \boldsymbol{r}^A(\xi^A) - \delta \boldsymbol{r}^B(\xi^B)\big)^T \delta \boldsymbol{r}^B_{,\xi}(\xi^B), \tag{28}$$

and Ω_c indicates the integration domain, i.e., the contact patch to be constrained on the contacting surface of the slave (A) and master (B) beams, and p_n is the penalty parameter. The vector of the distributed contact forces can be identified in Eq. (27) in the form of

$$\boldsymbol{f}_{\text{con}} = \underbrace{p_n\, g\big(\xi^A, \xi^B(\xi^A)\big)}_{f_{\text{con}}} \boldsymbol{n}\big(\xi^A, \xi^B(\xi^A)\big), \tag{29}$$

where f_{con} is the average magnitude of action-reaction contact pressure on the entire surface of the contact region and

$$\boldsymbol{n}\big(\xi^A, \xi^B_c(\xi^A)\big) = \frac{\boldsymbol{r}^B\big(\xi^B_c(\xi^A)\big) - \boldsymbol{r}^A(\xi^A)}{\left\|\boldsymbol{r}^B\big(\xi^B_c(\xi^A)\big) - \boldsymbol{r}^A(\xi^A)\right\|} \tag{30}$$

is the contact normal vector.

4.1.2. Contact patch segmentation

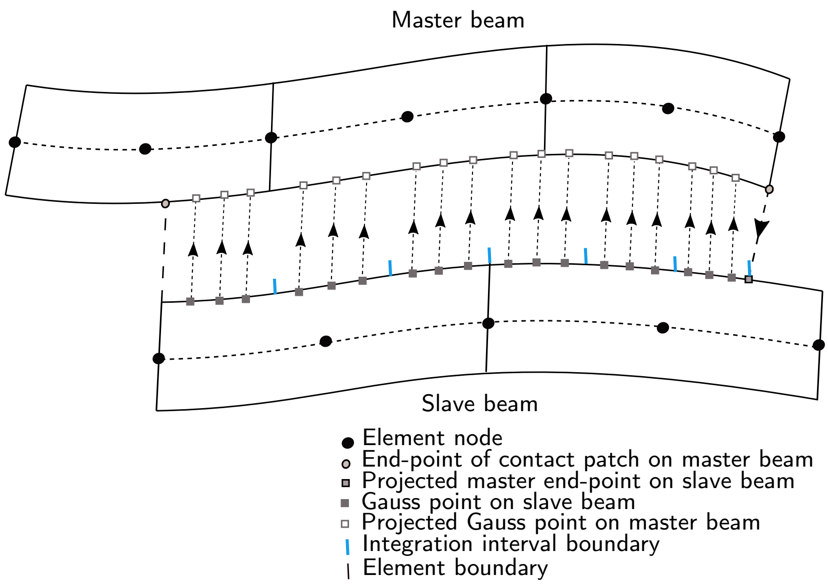

Figure 3: Illustration of integration segmentation along the contact patch in the contacting master and slave beams.

The weak form of contact energy (27) can be expressed in discretized form by substituting the position vector $\boldsymbol{r}$

from Eq. (4) into Eq. (27) as follows:

$$\begin{aligned}\delta\Pi_{\text{con}} &= -\delta \boldsymbol{u}^{A,T}\underbrace{p_n\sum_{j=1}^{n_G} g\big(\xi_j^A,\xi_c^B(\xi_j^A)\big)\mathbf{N}^T(\xi_j^A)\boldsymbol{n}\big(\xi_j^A,\xi_c^B(\xi_j^A)\big)w_j\boldsymbol{J}(\xi_j^A)}_{\boldsymbol{f}^A_{\text{con}}(\xi_j^A)} \\ &+ \delta\boldsymbol{u}^{B,T}\cdot\underbrace{p_n\sum_{j=1}^{n_G} g\big(\xi_j^A,\xi_c^B(\xi_j^A)\big)\mathbf{N}^T\left(\xi_c^B(\xi_j^A)\right)\boldsymbol{n}\big(\xi_j^A,\xi_c^B(\xi_j^A)\big)w_j\boldsymbol{J}\left(\xi_c^B(\xi_j^A)\right)}_{\boldsymbol{f}^B_{\text{con}}\left(\xi_c^B(\xi_j^A)\right)}.\end{aligned} \tag{31}$$

In Eq. (31), n_G^j is the number of the Gauss points along a slave element's centre line, w_j is the weight of the j^{th} Gauss point, ξ_j is the j^{th} Gauss points coordinate in terms of the slave beam parameter ξ^A, $\xi^B(\xi_j^A)$ are the closest projected master point assigned to the slave Gauss point parameter ξ_j^A and $\boldsymbol{J}(\xi_j^A)$ and $\boldsymbol{J}\left(\xi_c^B(\xi_j^A)\right)$ are the scaling factor between the increment of the Gauss point coordinates in the bi-normalized and the physical coordinate systems in the slave and master beam. Terms specified by $\boldsymbol{f}^A_{\text{con}}(\xi_j^A)$ and $\boldsymbol{f}^B_{\text{con}}\left(\xi_c^B(\xi_j^A)\right)$ represent the vector of distributed contact reaction forces corresponding to the slave and master elements, respectively. The integration interval used in Eq. (31) can be further parameterized by assigning n_S segments to each beam slave element. Therefore, for n_S number of segments within a slave element, the new coordinate parameter in a slave beam element can be expressed with respect to the interpolation

$$\xi_{sj}^A = \xi_s^A(\xi_j^A) = \frac{\xi_{s,2e}^A - \xi_{s,1e}^A}{2}\xi_j^A + \frac{\xi_{s,2e}^A + \xi_{s,1e}^A}{2}, \quad \text{for } j = 1,...,n_G, \text{ for } s = 1,...,n_S, \tag{32}$$

where $\xi_{s,1e}^A$ and $\xi_{s,2e}^A$ are the integration boundaries at each integration segment. The further parameter ξ_s^A is equidistantly spaced within the intervals $[-1,1]$ unless there exists a valid projection for a master beam endpoint $\boldsymbol{r}^B\big(\xi^B_{s,1e/s,2e}(\xi^A)\big)$ on a slave element according to Eq. (24), that is to be iteratively solved via the following closest projected point problem

$$h_1(\xi_{1e}^A,\xi_{1c}^B) = 0 \quad \text{and} \quad h_1(\xi_{2e}^A,\xi_{2c}^B) = 0, \tag{33}$$

where ξ_{1c}^B and ξ_{2c}^B are the abscissa coordinate of the master beam end-points. Figure 3 illustrates the projection of the Gauss points on the corresponding closest master element for $n_S = 3$. Now the discretized contact energy variation (31) can be expressed with a further parameterization consisting of the beam discretization (4), and the contact segmentation (32) written in the form of two sums over the number of Gauss points and over the integral segments as follows:

$$\begin{aligned}\delta\Pi_{\text{con}} &= -\delta\boldsymbol{u}^{A,T}p_n\sum_{j=1}^{n_G}\sum_{s=1}^{n_S} g\big(\xi_{sj}^A,\xi_c^B(\xi_{sj}^A)\big)\mathbf{N}^T(\xi_{sj}^A)\boldsymbol{n}\big(\xi_{sj}^A,\xi_c^B(\xi_{sj}^A)\big)\cdot w_j\boldsymbol{J}(\xi_{sj}^A) \\ &+ \delta\boldsymbol{u}^{B,T}p_n\sum_{j=1}^{n_G}\sum_{s=1}^{n_S} g\big(\xi_{sj}^A,\xi_c^B(\xi_{sj}^A)\big)\mathbf{N}^T\left(\xi_c^B(\xi_{sj}^A)\right)\boldsymbol{n}\big(\xi_{sj}^A,\xi_c^B(\xi_{sj}^A)\big)\cdot w_j\boldsymbol{J}\left(\xi_c^B(\xi_{sj}^A)\right),\end{aligned} \tag{34}$$

where

$$J(\xi_{sj}^A) = \frac{\partial\boldsymbol{r}(1)^A}{\partial\xi^A}\frac{\partial\xi^A}{\partial\xi_s^A} = H^A W^A\frac{L^A}{2}\frac{\xi_{s,2e}^A - \xi_{s,1e}^A}{2}, \tag{35}$$

in which L^A and W^A are the slave beam length and width.

Remark 2. *Perhaps the presented line-to-line formulation is analogous to the modified virtual slave node-to-segment formulation introduced in [57] that the original virtual slave node-to-segment formulation had been presented in [58]. In the modified formulation [57], the Gauss points distribution on a slave beam was replaced with the virtual points or nodes that are placed in the centroid of each contacting element's segment for a planar linear solid element. Comparing to the so-called algorithm " a modified node-to-segment algorithm passing contact patch test (VTS-PPT), the introduced line-to-line and surface-to-surface formulations show an analogy up to a certain level. In particular, the abscissa displacements of the equally-spaced slave segments and their containing Gauss points are associated to a beam element's (end / middle) node via a linear interpolation given by Eq.* (32)*. On the other hand, the formulation in this work differs from the NTS-PPT with respect to the following points. In the introduced line-to-line and surface-to-surface formulations, the resultant of contact pressure acting from each of slave segments denoted* f_N *in Eq.* (29)*, is distributed over a projected area on the master surface (i.e., element) as shown by Figure 3, which ultimately, is transferred into a master node's degrees-of-freedom. Conversely, with the NTS-PPT algorithm, the resultant of the contact pressure acting from a slave segment will finally be transferred to the master end nodes in the master surface involving the projected area as equivalent concentrated nodal forces in the normal direction.*

4.2. Surface-to-surface contact formulation

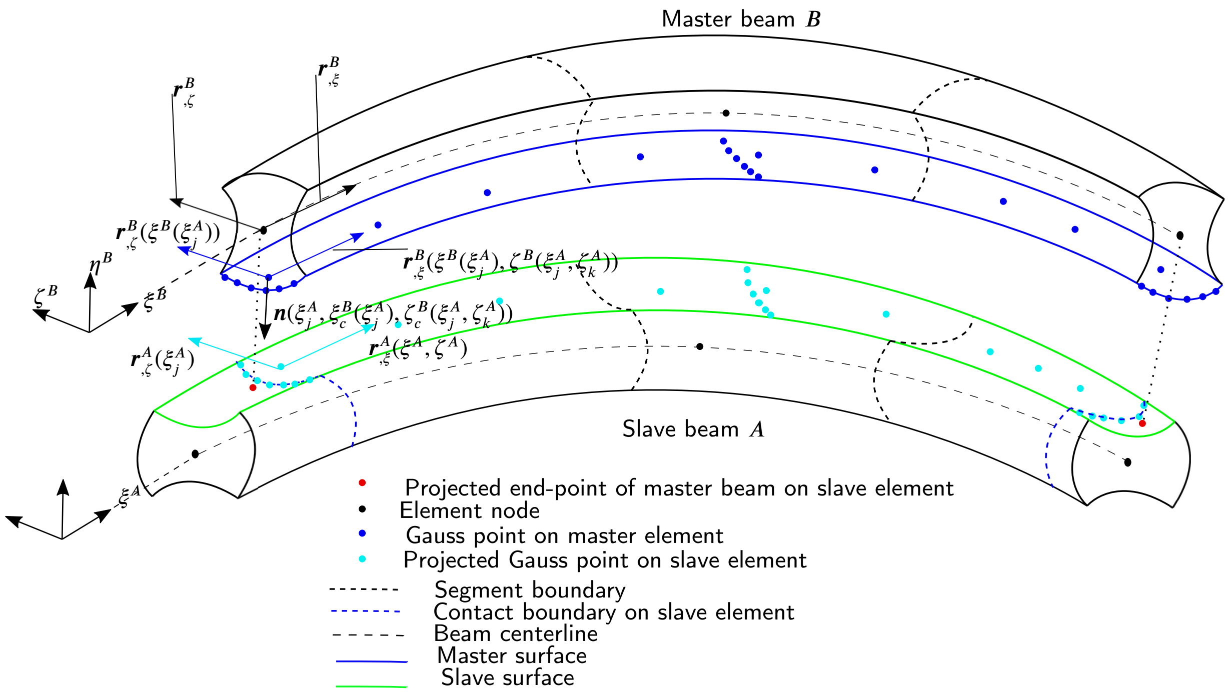

Figure 4: Kinematic parameters of a beam surface-to-surface contact problem

In this section, the described line-to-line formulation in Section 4.1 is extended into a beam surface-to-surface contact formulation. The introduced formulation is developed to be applied in both external and internal beam contact configurations. The internal contact description of the formulation is particularly developed to take advantage of the solid-like features of the continuum based ANCF beam that is integrated with the introduced cross-section approximation scheme in Section 3.

4.2.1. External contact description

The unilateral minimum problem defined by Eq. (23) is now adapted to measure the minimum distance field between the closest vector field

$$\boldsymbol{r}_c^B\Big(\xi_c^B(\xi^A), \zeta_c^B\big(\xi^B(\xi^A), \zeta^A\big)\Big) \equiv \boldsymbol{r}_c^B\big(\xi_c^B, \zeta_c^B(\xi_c^B)\big), \tag{36a}$$

defining the portion of contact surface of on beam B (master), and the position vector field

$$\boldsymbol{r}^A\big(\xi^A, \zeta^A(\xi^A)\big) \equiv \boldsymbol{r}^A(\xi^A, \zeta^A) \tag{36b}$$

that belongs to beam A (slave) surface. Hereafter, according to the equivalence expressions (36), the notations for coordinate parameters ξ_c^B and ζ_c^B will be simplified. As implicitly pointed out with the expressions (36), the transverse coordinate ζ^A is the solutions to the following closest projection point problems

$$p_1\big(\zeta^A(\xi^A)\big) = \Big(\boldsymbol{r}^A\big(\xi^A, \zeta^A(\xi^A, \eta^A)\big) - \boldsymbol{r}_f^A(\xi^A, \zeta^A)\Big)^T \boldsymbol{r}^A_{,\xi}\big(\xi^A, \zeta^A(\xi^A, \eta^A)\big) = 0, \tag{37}$$

where

$$\boldsymbol{r}_f^A(\xi^A, \eta^A, \zeta^A) = \mathbf{N}(\xi^A, \eta^A, \zeta^A)\boldsymbol{q}^A \tag{38}$$

is the position vector field of the Gauss points defining the cross-section of a slave beam element.

Remark 3. *The normal projection* (37) *is performed to assure that the vector field* $\boldsymbol{r}^A\big(\xi^A, \zeta^A(\xi^A, \eta^A)$ *represents the contact points candidate in terms of the deformation-dependent coordinate parameter* $\zeta^A(\xi^A)$.

The minimum distance problem between the vector fields (36) is in the form of

$$d\big(\zeta^A, \zeta_c^B(\xi_c^B, \zeta^A)\big) := \min_{\zeta^B(\xi^A, \zeta^A)} d(\zeta^A, \zeta^B) = \left\|\boldsymbol{r}^A(\xi^A, \zeta^A) - \boldsymbol{r}_c^B(\xi_c^B, \zeta_c^B)\right\|, \tag{39}$$

in which again, assuming contact takes place across a surface with $\eta_c^B = -1$ and $\eta_c^A = 1$ in the current configuration, the further orthogonality condition in addition to Eq. (24) in the case of the line-to-line contact model, is in the following structure

$$\begin{aligned} p_2(\zeta^A, \zeta^B) &= \Big(\boldsymbol{r}^B\big(\xi^B(\xi^A), \zeta^B(\xi^A, \zeta^A)\big) - \boldsymbol{r}_f^A(\xi^A, \eta^A, \zeta^A)\Big)^T \boldsymbol{r}^B_{,\zeta}\big(\xi^B(\xi^A), \zeta^B(\xi^A, \zeta^A)\big) \\ &\text{with } \; p_2\Big(\zeta^A, \zeta_c^B\big(\xi_c^B(\xi^A), \zeta^A\big)\Big) = 0, \end{aligned} \tag{40}$$

where $\boldsymbol{r}^B_{,\zeta}(\xi^B, \zeta^B)$ is the derivation of the position vector beam B with respect to local coordinate parameter ζ^A. The gap function field $g\big(\xi^A, \xi^B(\xi^A), \zeta^A, \zeta^B(\xi^A, \zeta^A)\big)$ is defined to express the non-penetration condition

$$\begin{aligned} g(\xi^A, \xi^B, \zeta^A, \zeta^B) = d\big(\boldsymbol{\xi}^A(\xi^A, \zeta^A), \boldsymbol{\xi}^B(\xi_c^B, \zeta_c^B)\big) &= \left\|\boldsymbol{r}^A(\xi^A)_{\eta,\zeta=0} - \boldsymbol{r}^B(\xi_c^B)_{\eta,\zeta=0}\right\| \\ - \Big(\left\|\boldsymbol{r}^A(\xi^A, \zeta^A) - \boldsymbol{r}^A(\xi^A)_{\eta,\zeta=0}\right\| &+ \left\|\boldsymbol{r}_c^B\big(\xi_c^B, \zeta_c^B(\xi_c^B)\big) - \boldsymbol{r}^B(\xi_c^B)_{\eta,\zeta=0}\right\|\Big) \text{ with } g(\xi^A, \xi^B, \zeta^A, \zeta^B) \geq 0. \end{aligned} \tag{41a}$$

Similar to the line-to-line formulation in Section 4.1, the variation of contact energy due to the surface-to-surface contact then reads as follows:

$$\delta\Pi_{\text{con}} = p_n \int_{\Omega_c} g(\xi^A, \xi^B, \zeta^A, \zeta^B)\delta g(\xi^A, \xi^B, \zeta^A, \zeta^B)\, \mathrm{d}\Omega_c, \tag{42}$$

where Ω_c denotes the integration over the projected area on the both slave and master beams external surface. According to the kinematics demonstrated in Figure 4, the contact normal vector is defined as the cross product of the tangent vectors

$$\boldsymbol{\tau}(\zeta^B) = \frac{\partial \boldsymbol{r}^B}{\partial \zeta^B} \tag{43}$$

and

$$\boldsymbol{\xi}^B(\xi^B, \zeta^B) = \frac{\partial \boldsymbol{r}^B}{\partial \xi^B} \tag{44}$$

with respect to the beam local coordinate ζ^B and ξ^B, respectively. The contact normal vector from the master element surface to the slave element surface is then

$$\boldsymbol{n}(\xi^B, \zeta^B) = \frac{\boldsymbol{\xi}^B(\xi^B, \zeta^B) \times \boldsymbol{\tau}(\zeta^B)}{\left\| \boldsymbol{\xi}^B(\xi^B, \zeta^B) \times \boldsymbol{\tau}(\zeta^B) \right\|}. \tag{45}$$

It is known that similar to the definition of the contact normal vector in Section 4, the normal vector in the surface-to-surface contact description is perpendicular to the master beam centre line, and is not necessarily perpendicular to the slave element. The contact normal vector defined by Eq. (45) can alternatively be calculated similar to that of the line-to-line formulation given by Eq. (30). Hereon, the contact vector is in the form of

$$\boldsymbol{n}\Big(\xi^A, \xi_c^B(\xi^A), \zeta_c^B\left(\xi_c^B(\xi^A), \zeta^A\right)\Big) = \frac{\boldsymbol{r}^B(\xi_c^B, \zeta_c^B) - \boldsymbol{r}^A(\xi^A, \zeta^A)}{\left\| \boldsymbol{r}^B(\xi_c^B, \zeta_c^B) - \boldsymbol{r}^A(\xi^A, \zeta^A) \right\|}. \tag{46}$$

Remark 4. *The contact normal vector given by Eq. (46) is analogous to that in the case of the line-to-line formulation that appeared in Section 4.1 (see Eq. (30)). The above-mentioned contact normal is preferred over (45) which is defined similarly to that in [59] in the implementation of the introduced formulation in this work.*

4.2.2. External contact surface segmentation

The discretized form of contact energy (31) can be parameterized in the transverse directions η or ζ that herein the η direction is abstained without loss of generality and consistency. It is assumed that contact between the beams takes place in between the upper surface of beam A (slave), and the lower surface of beam B (master), see Figure 4. Analogous to Section 4.1.2, the variation of contact energy is of the following form:

$$\begin{aligned}\delta\Pi_{\text{con}} = &-\delta \boldsymbol{u}^{A,T} p_n \sum_{j=1}^{n_G^j} \sum_{k=1}^{n_G^k} g\big((\xi_c^B(\xi_j^A), \zeta_c^B(\xi_j^A, \zeta_k^A)\big) \mathbf{N}^T(\xi_j^A, \zeta_k^A) \boldsymbol{n}\big(\xi_j^A, \xi_c^B(\xi_j^A), \zeta_c^B(\xi_j^A, \zeta_k^A)\big) w_j w_k \boldsymbol{J}(\xi_j^A, \zeta_k^A)\\ &+ \delta \boldsymbol{u}^{B,T} p_n \sum_{j=1}^{n_G^j} \sum_{k=1}^{n_G^k} g\big((\xi_c^B(\xi_j^A), \zeta_c^B(\xi_j^A, \zeta_k^A)\big) \mathbf{N}^T\left((\xi_c^B(\xi_j^A), \zeta_c^B(\xi_j^A, \zeta_k^A)\right) \boldsymbol{n}\big(\xi_j^A, \xi_c^B(\xi_j^A), \zeta_c^B(\xi_j^A, \zeta_k^A)\big)\\ &\cdot w_j w_k \boldsymbol{J}\left(\xi_c^B(\xi_j^A), \zeta_c^B(\xi_j^A, \zeta_k^A)\right).\end{aligned} \tag{47}$$

In Eq. (47), n_G^k is the number of Gauss points in a slave element, along the cross-section border in ζ direction, w_k are the corresponding Gauss points weight, ζ_k are the Gauss points coordinate in terms of the slave beam parameters ξ^A and ζ^A, $\zeta_c^B(\xi_j^A, \zeta_k^A)$ is the closest projected master point assigned to the Gauss slave point parameters ξ_j^A and ζ_k^A, and $\boldsymbol{J}(\xi_j^A, \zeta_k^A)$ and $\boldsymbol{J}\left(\xi_c^B(\xi_j^A), \zeta_c^B(\xi_j^A, \zeta_k^A)\right)$ are the scaling factor between the increment of the Gauss point coordinates in the bi-normalized and the physical coordinate systems in the slave and master beam, respectively. For n_S number of segments within a slave element, the variation of discretized contact energy can be expressed with an additional integration along the transverse direction ζ, using the coordinate parameter ζ_k as follows:

$$\begin{aligned}\delta\Pi_{\text{con}} =& -\delta\boldsymbol{u}^{A,T} p_n \sum_{k=1}^{n_G^k}\sum_{j=1}^{n_G^j}\sum_{s=1}^{n_S} g\big((\xi_c^B(\xi_{sj}^A),\zeta_c^B(\xi_{sj}^A,\zeta_k^A)\big)\mathbf{N}^T(\xi_{sj}^A,\zeta_k^A)\boldsymbol{n}\big(\xi_{sj}^A,\xi_c^B(\xi_{sj}^A),\zeta_c^B(\xi_{sj}^A,\zeta_k^A)\big)w_j w_k \boldsymbol{J}(\xi_{sj}^A,\zeta_k^A)\\ &+\delta\boldsymbol{u}^{B,T} p_n \sum_{k=1}^{n_G^k}\sum_{j=1}^{n_G^j}\sum_{s=1}^{n_S} g\big((\xi_c^B(\xi_{sj}^A),\zeta_c^B(\xi_{sj}^A,\zeta_k^A)\big)\mathbf{N}^T\big((\xi_c^B(\xi_{sj}^A),\zeta_c^B(\xi_{sj}^A,\zeta_k^A)\big)\boldsymbol{n}\big(\xi_{sj}^A,\xi_c^B(\xi_{sj}^A),\zeta_c^B(\xi_{sj}^A,\zeta_k^A)\big)\\ &\cdot w_j w_k \boldsymbol{J}\big(\xi_c^B(\xi_{sj}^A),\zeta_c^B(\xi_{sj}^A,\zeta_k^A)\big).\end{aligned} \tag{48}$$

where

$$\boldsymbol{J}(\xi_{sj}^A,\zeta_k^A) = \frac{\partial \boldsymbol{r}^A(1)}{\partial \xi^A}\frac{\partial \zeta^A}{\partial \xi_s^A}\frac{\partial \boldsymbol{r}^A(3)}{\partial \zeta^A} = H^A\frac{L^A}{2}\frac{\xi_{s,2e}^A-\xi_{s,1e}^A}{2}\frac{W^A}{2}. \tag{49}$$

Remark 5. *In the implementation of the parameterized contact contribution (48), two loops are sufficient enough to go through the integration patches. One loop imposes the contact constraint on each of ξ_{sj}^A and $\xi_c^B(\xi_{sj}^A)$ simultaneously in a collocation manner, and the second one imposes the corresponding contact constraint for n_G^k number of Gauss points corresponding to each ξ_{sj}^A and $\xi_c^B(\xi_{sj}^A)$, see Algorithm 1.*

4.2.3. Internal contact description

Description of the surface-to-surface contact presented in Section 4.2.1 is slightly adapted for the configurations in which the internal contact exists. An essential difference between the external and internal contact descriptions in this work is that in the case of the internal contact, at least one of the contact pairs (a master or a slave beam), comes into contact with its inner surface where none of the transverse coordinate parameters η or ζ are located on the external surface of the contacting beam, i.e. $\eta,\zeta \neq \{-1,1\}$. This means that in addition to the position vector fields (36), the following position vector fields are expressed in terms of coordinates η^A and η^B such that

$$\boldsymbol{r}_c^B\Big(\xi_c^B(\xi^A),\zeta_c^B\big(\xi^B(\xi^A),\zeta^A\big),\eta_c^B\big(\xi^B(\xi^A)\big),\eta^A\Big) \equiv \boldsymbol{r}_c^B\big(\xi_c^B,\eta_c^B(\xi_c^B),\zeta_c^B(\xi_c^B)\big) \tag{50a}$$

and

$$\boldsymbol{r}^A\big(\xi^A,\eta^A(\xi^A),\zeta^A(\xi^A)\big) \equiv \boldsymbol{r}^A(\xi^A,\eta^A,\zeta^A) \tag{50b}$$

defining the portion of contact surface on beam B (master), and the position vector field belongs to beam A (slave) surface in an internal contact scenario. The notations for coordinate parameters η_c^B and η^A will also be simplified in the rest of the paper. Similar to the external contact description, the following additional closest projection point problems have to be solved for the transverse coordinates η^A and η^B. The transverse coordinate parameters on the slave beam is given by solving the following projection point problem

$$p_3\big(\eta^A(\xi^A)\big) = \big(\boldsymbol{r}^A\big(\xi^A,\eta^A(\xi^A,\zeta^A) - \boldsymbol{r}_f^A(\xi^A,\eta^A,\zeta^A)\big)^T \boldsymbol{r}_{,\xi}^A\big(\xi^A,\eta^A(\xi^A,\zeta^A)\big) = 0, \tag{51}$$

Again, the following minimum distance problem between the vector fields (50)

$$d(\eta^A,\eta_c^B) := \min_{\eta^A,\eta^B} d(\eta^A,\eta^B) = \left\|\boldsymbol{r}^A(\xi^A,\eta^A,\zeta^A) - \boldsymbol{r}_c^B(\xi_c^B,\eta_c^B,\zeta_c^B)\right\| \tag{52}$$

requires the solving of an additional closest projection problem for the unknown η_c^B which is not constant anymore in the case of an internal contact. So

$$p_4(\eta^A,\eta^B) = \big(\boldsymbol{r}^B\big(\xi^B(\xi^A),\eta^B(\xi^A,\eta^A) - \boldsymbol{r}_f^A(\xi^A,\eta^A,\zeta^A)\big)^T \boldsymbol{r}_{,\eta}^B\big(\xi^B(\xi^A),\eta^B(\xi^A,\eta^A)\big) \text{ with } p_4\Big(\eta^A,\eta_c^B\big(\xi_c^B(\xi^A),\eta^A\big)\Big) = 0$$

(53)

is to be solved along with Eq. (40). The gap function g in terms of the slave and master beam local parameters is defined to express the non-penetration condition

$$g(\xi^A, \xi^B, \eta^A, \eta^B, \zeta^A, \zeta^B) = d\big((\xi^A, \eta^A, \zeta^A), (\xi^B_c, \eta^B_c, \zeta^B_c)\big) = g_0 - \left\| \boldsymbol{r}^B_c\big(\xi^B_c, \eta^B_c(\xi^B_c), \zeta^B_c(\xi^B_c)\big) - \boldsymbol{r}^A(\xi^A, \eta^A, \zeta^A) \right\|$$
$$\text{with } g(\xi^A, \xi^B, \eta^A, \eta^B, \zeta^A, \zeta^B) \geq 0, \tag{54a}$$

where g_0 is an initial gap in a beam-inside-beam configuration. The normal vector in the internal contact is prescribed similar to (46) and is expressed in terms of Eqs. (50) as follows:

$$\boldsymbol{n}\big(\xi^A, \xi^B_c, \eta^B_c(\xi^B_c), \zeta^B_c(\xi^B_c)\big) = \frac{\boldsymbol{r}^B_c\big(\xi^B_c, \eta^B_c(\xi^B_c), \zeta^B_c(\xi^B_c)\big) - \boldsymbol{r}^A(\xi^A, \eta^A, \zeta^A)}{\left\| \boldsymbol{r}^B_c\big(\xi^B_c, \eta^B_c(\xi^B_c), \zeta^B_c(\xi^B_c)\big) - \boldsymbol{r}^A(\xi^A, \eta^A, \zeta^A) \right\|}. \tag{55}$$

4.2.4. Internal contact surface segmentation

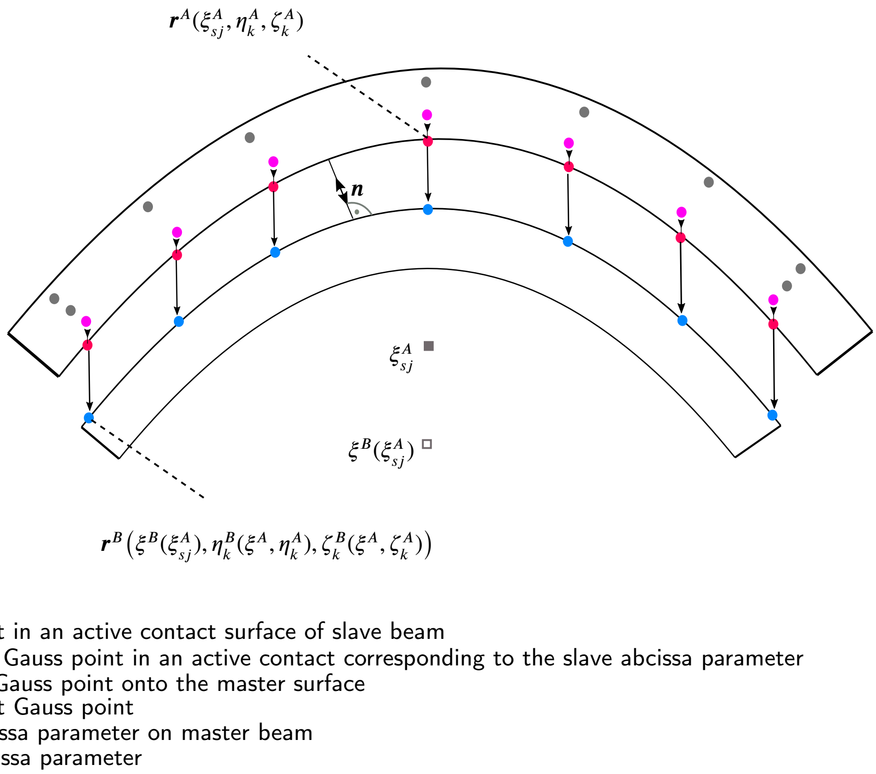

Figure 5: Illustration of the definition of the parameterized contacting surfaces in an internal contact description. The procedure of treatment of the Gauss points candidates on an active slave beam's internal surface and their projection on the master beam's external surface is shown.

The discretized form of contact energy (31) can be parameterized in the transverse directions η or ζ that herein the η direction is also accounted for in the parametrization. An internal contact within the beams takes place such that the internal surface of the upper beam B (master) comes into contact with the external surface of the lower beam beam A (slave), see Figure 5. The variation of contact energy is expressed as

$$\begin{aligned}\delta\Pi_{\text{con}} = &-\delta\boldsymbol{u}^{A,T} p_n \sum_{j=1}^{n_G^j}\sum_{k=1}^{n_G^k} g\big((\xi^B(\xi_j^A), \eta^B(\xi_j^A,\eta_k^A), \zeta^B(\xi_j^A,\zeta_k^A)\big)\mathbf{N}^T(\xi_j^A,\eta_k^A,\zeta_k^A)\\ &\cdot \boldsymbol{n}\big(\xi^A, \xi_c^B, \eta_c^B\big(\xi_c^B\big), \zeta_c^B\big(\xi_c^B\big)\big) w_j w_k \boldsymbol{J}(\xi_j^A,\eta_k^A,\zeta_k^A)\\ &+\delta\boldsymbol{u}^{B,T} p_n \sum_{j=1}^{n_G^j}\sum_{k=1}^{n_G^k} g\big((\xi^B(\xi_j^A), \eta^B(\xi_j^A,\eta_k^A), \zeta^B(\xi_j^A,\zeta_k^A)\big)\mathbf{N}^T\big((\xi^B(\xi_j^A), \eta^B(\xi_j^A,\eta_k^A), \zeta^B(\xi_j^A,\zeta_k^A)\big)\\ &\cdot \boldsymbol{n}\big(\xi^A, \xi_c^B, \eta_c^B\big(\xi_c^B\big), \zeta_c^B\big(\xi_c^B\big)\big) w_j w_k \boldsymbol{J}(\xi_j^B,\eta_k^B,\zeta_k^B).\end{aligned} \tag{56}$$

In Eq. (56), n_G^k is again the number of Gauss points in a slave element in the directions along the internal surface of the cross-section in terms of the transverse coordinates η and ζ, η_k is the Gauss point coordinate in terms of the slave beam parameters ξ^A, $\eta^B(\xi_j^A, \zeta_j^A)$ is the closest projected master point assigned to the Gauss slave point parameters ξ_j^A and ζ_k^B, $\boldsymbol{J}(\xi_j^A,\eta_k^A,\zeta_k^A)$ and $\boldsymbol{J}(\xi_j^B,\eta_k^B,\zeta_k^B)$ are the scaling factor between the bi-normalized and the physical coordinate systems in terms of the Gauss point coordinates in the slave and master beams, respectively. Again, the integration interval used in Eq. (56) can be further parameterized by assigning n_S segments for each beam slave element. Therein, for n_S number of segments within a slave element, the variation of discretized contact energy can be expressed with an additional integration patch along the transverse direction, i.e., along the splines defining the cross-section portion that is in contact. The parameterized contact energy contribution to Eq. (12) reads according to the following structure:

$$\begin{aligned}\delta\Pi_{\text{con}} = &-\delta\boldsymbol{u}^{A,T} \sum_{k=1}^{n_G^k}\sum_{j=1}^{n_G^j}\sum_{s=1}^{n_S} g\big(\xi^B(\xi_{sj}^A), \eta_k^B(\xi_{sj}^A,\eta_k^A), \zeta_k^B(\xi_{sj}^A,\zeta_k^A)\big)\mathbf{N}^T\big(\xi_{sj}^A, \eta_k^A(\xi^A), \zeta_k^A(\xi^A)\big)\\ &\cdot \boldsymbol{n}\big(\xi_{sj}^A, \xi^B(\xi_{sj}^A), \eta^B(\xi_{sj}^A,\eta_k^A), \zeta^B(\xi_{sj}^A,\zeta_k^A)\big) w_j w_k \boldsymbol{J}\big(\xi_{sj}^A, \eta_k^A(\xi^A), \zeta_k^A(\xi^A)\big)\\ &+\delta\boldsymbol{u}^{B,T} \sum_{k=1}^{n_G^k}\sum_{j=1}^{n_G^j}\sum_{s=1}^{n_S} g\big(\xi^B(\xi_{sj}^A), \eta_k^B(\xi_{sj}^A,\eta_k^A), \zeta_k^B(\xi_{sj}^A,\zeta_k^A)\big)\mathbf{N}^T\big(\xi^B(\xi_{sj}^A), \eta_k^B(\xi_{sj}^A,\eta_k^A), \zeta_k^B(\xi_{sj}^A,\zeta_k^A)\big)\\ &\cdot \boldsymbol{n}\big(\xi_{sj}^A, \xi^B(\xi_{sj}^A), \eta^B(\xi_{sj}^A,\eta_k^A), \zeta^B(\xi_{sj}^A,\zeta_k^A)\big) w_j w_k \boldsymbol{J}\big(\xi_{sj}^A, \eta_k^A(\xi^A), \zeta_k^A(\xi^A)\big),\end{aligned} \tag{57}$$

where

$$\boldsymbol{J}\big(\xi_{sj}^A, \eta_k^A(\xi^A), \zeta_k^A(\xi^A)\big) = \frac{\partial \boldsymbol{r}^A(1)}{\partial \xi^A}\frac{\partial \xi^A}{\partial \xi_s^A}\frac{\partial \boldsymbol{r}^A(2)}{\partial \eta^A}\frac{\partial \boldsymbol{r}^A(3)}{\partial \zeta^A} = \frac{L^A}{2}\frac{\xi_{2e}^A - \xi_{1e}^A}{2} H^A \frac{W^A}{2}. \tag{58}$$

4.3. Arbitrary curve-to-curve contact in the surface-to-surface contact description

In this section, the contact between beams with elliptical cross-sections was described as an arbitrary curve-to-curve contact across the surface of the contacting beams when warping around each other. The contact points' candidates were identified on the contacting beam's surfaces using a local contact search algorithm at each beams' sections characterized by an abscissa and the two ordinate parameters (ξ_{sj},η_k,ζ_k) as illustrated in Fig 6. It follows the Euclid's distance check

$$d_{min} = \min\Big(\Big\|(\boldsymbol{r}^A(\xi_{sj}^A,\eta_k^A,\zeta_k^A) - \boldsymbol{r}\big(\xi_B(\xi_{sj}^A),\eta_l^B,\zeta_l^B\big)\Big\|\Big),\ \ j=1,2,...,n_G^j,\ s=1,2,...,n_S\ \ k=1,2,...,n_G^k,\ l=1,2,...,n_G^l \tag{59}$$

over the entirety of the contacting beams. When the closest points from two contacting curves' sections are identified by Eq. (59) (see Figure 6), a Newton's iterative scheme seeks for an ordinate parameter solution for a closest

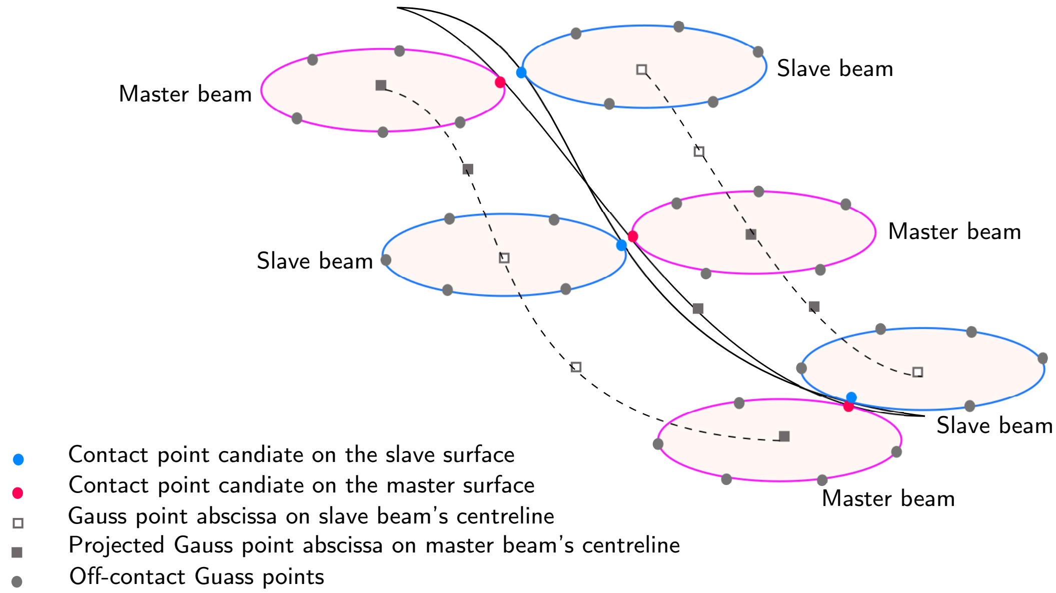

Figure 6: Illustration of the parameterized contact patch in a surface-to-surface contact description. The procedure of defining the contact point candidates on the active contact surface is shown for beams experience contact when wrapping around each other.

projection of the identified points belonging to the slave surface, onto the master surface. This task is accomplished by substituting the position vector

$$\boldsymbol{r}^A_{\min} = \boldsymbol{r}^A(\xi^A_{\min}, \eta^A_{\min}, \zeta^A_{\min}), \tag{60}$$

corresponding to contact point candidate on the slave surface, into Eqs. (40) and (53). Subsequently, the contact energy variation can be computed using the following line integral over the specified contact curves on each of the slave and master elements:

$$\begin{aligned} \delta\Pi_{\text{con}} = {} & \delta\boldsymbol{u}^{A,T} p_n \sum_{j=1}^{n_G}\sum_{s=1}^{n_S} g\big(\xi^B(\xi^A_{sj}), \eta^B_c, \zeta^B_c\big)\mathbf{N}^T(\xi^A_{sj}, \eta^A_c, \zeta^A_c)\boldsymbol{n}\big(\xi^B(\xi^A_{sj}), \eta^B_c, \zeta^B_c\big) w_j \boldsymbol{J}(\xi^A_{sj}) \\ & - \delta\boldsymbol{u}^{B,T} p_n \sum_{j=1}^{n_G}\sum_{s=1}^{n_S} g\big(\xi^B(\xi^A_{sj}), \eta^B_c, \zeta^B_c\big)\mathbf{N}^T\big(\xi^B(\xi^A_{sj}), \eta^B_c, \zeta^B_c\big)\boldsymbol{n}\big(\xi^B(\xi^A_{sj}), \eta^B_c, \zeta^B_c\big) w_j \boldsymbol{J}\big(\xi^B(\xi^A_{sj})\big), \end{aligned} \tag{61}$$

where η^A_c and η^B_c are respectively, the solutions of Eq. (51) and Eq. (53) when assigning position vector (60) to the slave and master elements, and similarly, ζ^A_c and ζ^B_c are the solutions after assigning vector (60) to Eqs. (37) and (40).

Remark 6. *The integrand in (61) is a parameterization of the contact energy over the helix like patch illustrated in Figure 6 within which the ordinate parameters η_c and ζ_c are deformation dependent on both the master and slave beams. This emanates from the fact that those ordinate parameters are solutions of Eqs. (51) and (53), locally solved using Newton's scheme.*

5. Numerical examples

In this section, the robustness, accuracy and performance of the beam surface-to-surface contact formulation presented in Section 4.2 are to be investigated by a number of contact problems. For all examples, the nonlinear

Newton's solver is used in order to solve Eq. (13) arising from the variational form of equations of equilibrium (12). A standard finite difference procedure is employed to evaluate the global tangent stiffness matrix (14) with the convergence criterion (16) during the numerical simulations. The total number of Gauss points per integration interval over each contact surface segment, is given by adding the Gauss points according to a Gauss rule with respect to the order of the contact energy function and those Gauss points across the portion of a cross-section in contact as follows:

$$n_G = \underbrace{\frac{r+1}{2}}_{n_G^j} + n_G^k \tag{62a}$$

with the total number of $n_{GT} = n_S \cdot n_G^j + n_G^k$ Gauss points per slave beam element, where r is the order of the integrating polynomial.

5.1. Contact patch test

The first example studies the performance and stability of the surface-to-surface contact formulation using a variant of the well-known patch test introduced in [60]. Figure 7 shows the configuration of the test with the modified boundary conditions for the upper beam A. The modification has to be made to apply a simply-supported boundary conditions in order to avoid the ill tangent stiffness matrix (i.e. low value of the condition number) in the static analysis performed. The material and geometrical parameters are collected in Table 1. The beams are made of a nearly-incompressible material model with respect to the Neo-Hookean model [51]. As discussed in [7], a contact algorithm can pass the patch test if the contact pressure magnitude within the numerical integration of the contact energy potential (42), (i.e., it can be identified analogously to (29)) can be equal to a constant normal traction f_{con} exerting on the contacting surfaces that must remain constant throughout the contact patch. Figure 9 plots the evolution of the contact pressure acting on both the contacting surfaces of beams in terms of length of the contact patch. In the figure, each data point represents the magnitude of the contact pressure associated with each integration segment. It is evidenced by the figure that with increasing the number of (total) segments within the contact region, the contact pressure is getting converged towards an almost constant value (48 segments). It should be recalled that the fluctuations in the contact pressure in the left side of the contact patch can be ascribed to the pin-type constraint used in the left end of the upper beam (A). This hinders the axial displacement in left-end of the beam and induces an excessive normal pressure. The technique used with the VTS-PPT in [57] to transform the uniform contact pressure acting over the projected master surface into equivalent concentrated nodal forces brings about the equivalence of the momentum over each master segment/element, which in turn leads to passing the patch test. However, re-producing the three-dimensional variant of this technique here can lead to the abdicating of the master nodal degrees-of-freedom associating with the cross-section deformation. Moreover, there is no proof that the VTS-PPT algorithm could satisfy the inf–sup condition which have already satisfied that proves the stability of the introduced formulation in this study. The stability, on the other hand, is studied using the inf-sup test [61, 7]. To this end, the following inf-sup condition

$$\frac{\int_{\Omega_c} p_n g(\xi^A, \xi^B, \zeta^A, \zeta^B) \mathrm{d}\Omega_c}{h_s p_n \|\boldsymbol{u}\|} = \beta_{hs} > 0 \tag{63}$$

should be satisfied according to [7], where h_s is the integral segment size and β_{hs} is the inf-sup value. Fig. 8 shows the logarithmic values of the inf-sup with increasing of integration segments on the contact patch. After a slight increase of β_{hs} for $n_S = 3$, it is almost bounded overhead with a small rise for $n_S = 6$. Therefore, the inf-sup test is passed [61].

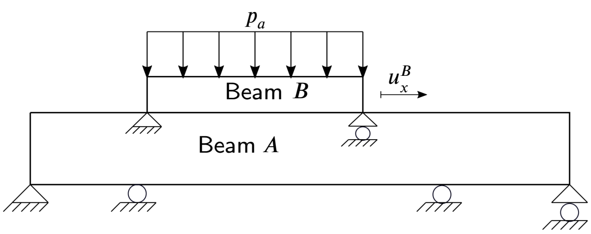

(a) Patch test problem with boundary conditions and loading. u_x^B is the axial displacement.

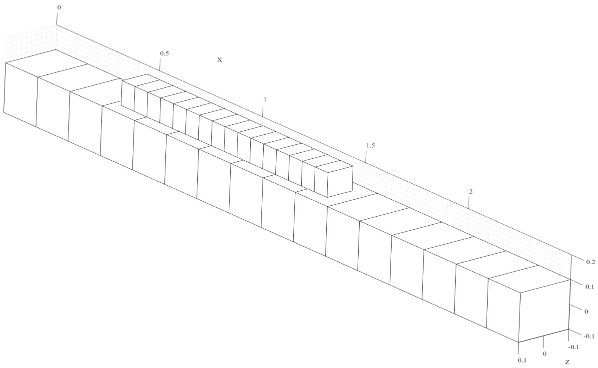

(b) Re-modelling of the Patch test using two geometrically different beams based on the ANCF. The beams are discretized using 16 elements made of the Neo-Hookean material.

Figure 7: Patch test illustration

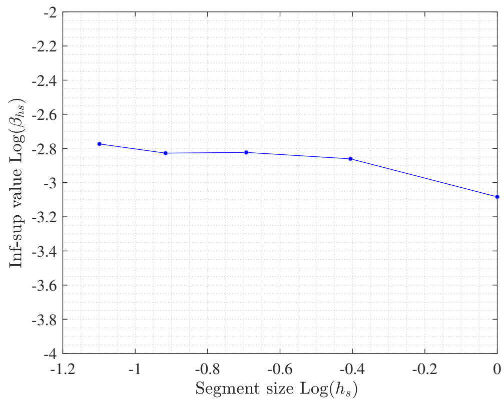

Figure 8: Inf-sup values for the contact patch test for increasing number of integration segments. The results are based on the discretization of 16 ANCF elements.

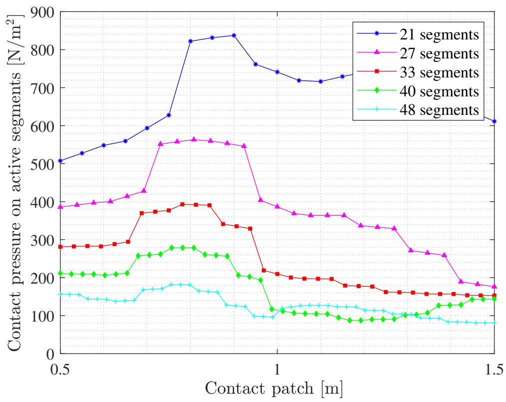

Figure 9: Contact pressure fields within contact patch in the patch test for increasing number of integration segments. The results are based on the discretization of eight ANCF elements when Neo-Hookean material is employed.

Table 1
Parameters of contact patch test

Parameters	Value
Young's modulus E [Pa]	$2.07 \cdot 10^9$
Poisson ratio ν	0.3
Penalty parameter p_n	10^6
External surface force p_a $[\frac{\mathrm{N}}{\mathrm{m}^2}]$	p_n
L^A [m]	2.5
L^B [m]	1
$H^A = W^A$ [m]	0.2
$H^B = W^B$ [m]	0.1

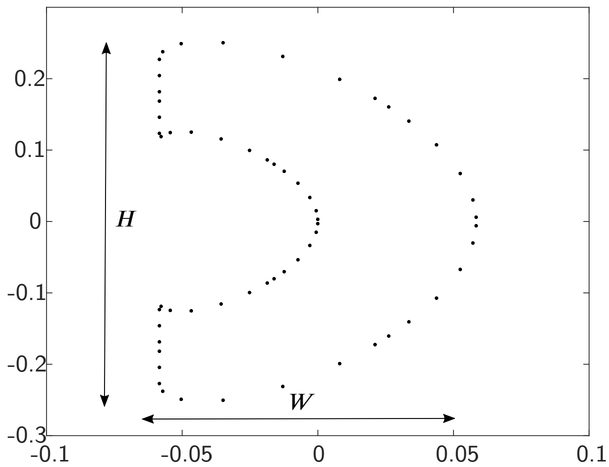

Figure 10: C-shape cross-section geometry after mapping the Gauss points coordinate from bi-normalised local coordinate to the physical local coordinate.

5.2. Bending problem - external contact

In this example, the performance and accuracy of the presented beam contact formulation is examined by considering a double cantilever beam problem. The example is inspired by the classical benchmark problem originally discussed in [59]. Due to the complicated non-symmetric beams cross-section in this example, the ambient pressure applied in the original problem in [59] is omitted. This is because of the fact that the imposition of the ambient pressure or more specifically, the bidirectional oppositely applied pressure on top of the upper beam and bottom of the lower beam on such a configuration would induce torsional moments that are the results of the non-symmetric beams cross-section. The lateral nodal degrees-of-freedom in the ANCF beam and similarly, the lateral surfaces in the 20-node solid element type in ABAQUS are constrained to avoid an instability problem. The material parameters used in the simulation are $E = 2.07 \cdot 10^{11}$ Pa and $\nu = 0.3$. The cross-section geometry with C-shape is shown in Figure 10 and the beams length are $L^A = L^B = 2$ m as shown in Table 2. The original material properties and geometrical parameters are changed to comply with the chosen cross-section shape, and with the ANCF beam internal force definition which was derived with respect to Eq. (18). The initial configuration of the structure is illustrated in Figure 11a. The structure underwent a large deformation at the end of the simulation at the maximum loading of $f_y = -10^9 \cdot H^3$, as shown in Figure 11b. In order to investigate the segmentation effect on the contacting

Table 2
External bending simulation parameters

Parameters	Value
Young's modulus E [Pa]	$2.07 \cdot 10^{11}$
Poisson ratio ν	0.3
External nodal force f_y [N]	$-10^9 \cdot H^3$
$L = L^A = L^B$ [m]	2

486 beams, a convergence analysis was done with an increasing number of segments on the contacting beam interface.

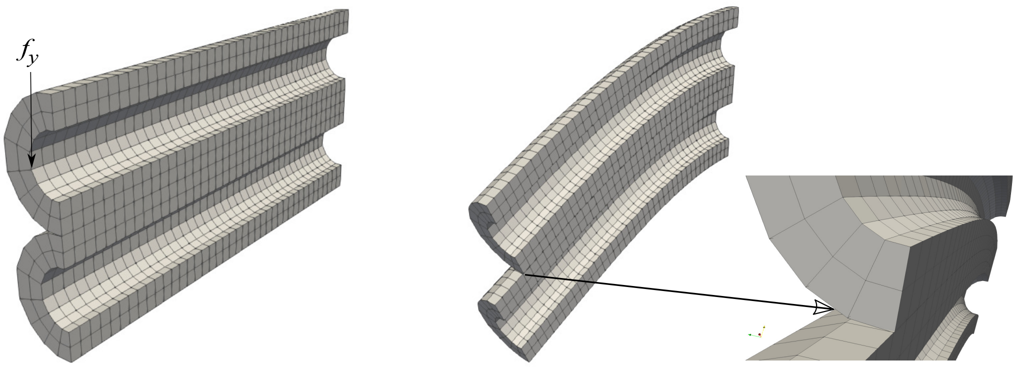

(a) Initial configuration (b) Deformed configuration

Figure 11: Bending of two beams with C-shape using discretization of eight beam elements

The rate of convergence of the norm of the contact reaction force applied from the slave beam (lower beam) in terms of the increasing number of total Gauss points on the entire slave beam's contacting surface is illustrated in Figure 12. The discretization used on the beam is eight ANCF beam elements and the total number of Gauss points n_{GT} increases according to Eq. (62) for ascending number of integration segments $n_S \in \{4, 6, 8, 10, 14\}$. The reference value is the norm of contact force when $n_S = 14$. It can be interpreted from Figure 12 that with increasing number of Gauss points, the relative error in the case of the slave beam's contribution to norm of vector of contact force is almost quadratically decreased and is minimized when $n_S = 10$. The converged solution for the norm of vector of contact force is associated with an acceptable small value for a relative error that was achieved with a low number of beam discretization. Moreover, as will be observed in Section 5.5, the relative error can also be mitigated by the increasing of number of beam discretization.

Figure 13 compares the convergence rate of solution for the end point's vertical displacement. Therein, the relative errors are expressed versus increasing number of the beam discretization $n_l \in \{3, 4, 8, 16, 24, 32\}$ to investigate the used beam element type performance. The relative errors for each beam discretization is computed with respect to the highest discretization (32 beam elements). It is evidenced by the figure that after some fluctuations at $n_l = 3$ and $n_l = 4$ where no converged solution is delivered, the solution converges almost quadratically at $n_l = 8$ at a sharp pace and afterward, the convergence rate follows a smoother trend. The diverged solutions at $n_l = 3$ and $n_l = 4$ can be explained by the fact that for low number of discretization, there is a positive gap distance between the candidate contacting elements in the region near to the beam clamped end under bending. This simply gives an inaccurate value for the vertical displacement, although the contact constraint are properly enforced where the contacting elements lie on each others. Nonetheless, the diverged solution at a very low beam discretization is expected from the ANCF beam's shape function interpolation under cross-sectional load cases, see [62] for a more specific

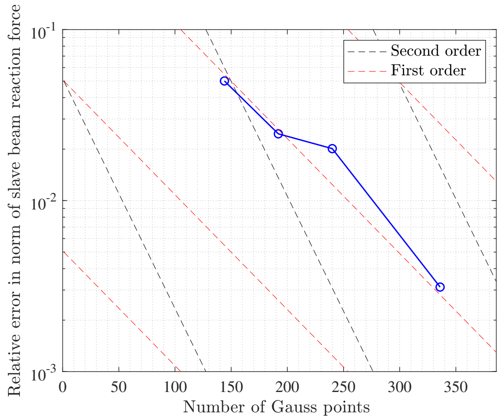

Figure 12: Rate of convergence of the double cantilever beam solution for the norm of the vector of contact (reaction) force $\left\|\boldsymbol{F}^{A}_{\text{con}}\right\|$ exerted from the slave beam with increasing number of Gauss points on entire of the slave beam. The dashed black and red lines indicate the second and first orders of convergence rate.

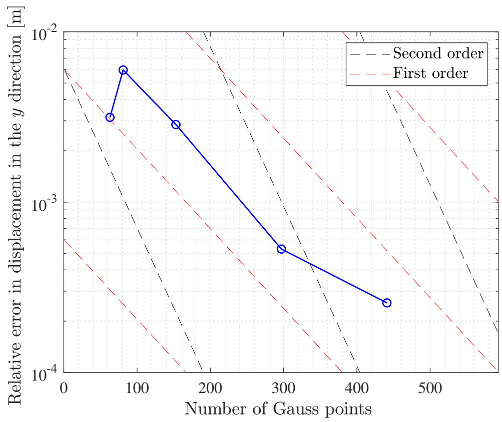

Figure 13: Rate of the convergence of the double cantilever beam's solution for end tip vertical displacement of the upper beam with increasing number of beam discretizations. The red and black dashed lines represent the first and second orders of the solution convergence rate.

discussion. For further investigation, the simulation was replicated in commercial finite element code ANSYS using a three-node beam element BEAM189. The contact elements options were set to replicate the used contact constraint enforcement in the proposed formulation. Therein, the contact model was chosen for parallel beam with distributed force, and the penalty method was chosen to enforce the contact constraint. Figure 14 shows the the lower beams centre line displacement based on the proposed contact formulation and the ANSYS solutions for the maximum loading. The results are based on eight ANCF elements with eight integration segments per element and 80 BEAM189 elements when nonlinear large static solver is selected. Although, the comparison between displacement of the two centre lines for the line-to-line and surface-to-surface formulations indicates a close agreement with BEAM189, they are not in strong agreement when compared with SOLID C3D8.

It can be explained that although the lateral degrees-of-freedom in all the four cases are constrained, it affects the solid element significantly more, this is because the Poisson effect is restricted in the lateral direction and does not induce more elongation and vertical displacement. This effect is less prominent in beam elements.

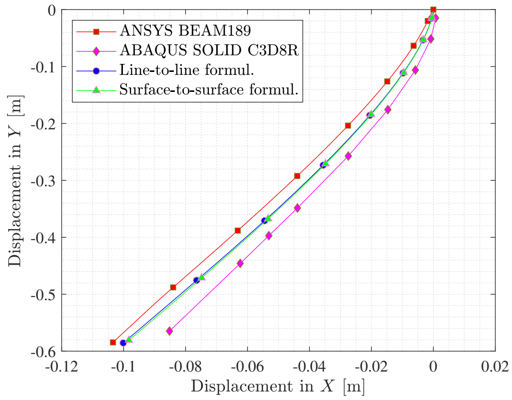

Figure 14: Comparison between the solutions for the slave beam centre line position using the proposed contact formulation, ANSYS and ABAQUS. A certain discretization of 16 of ANCF beams, 80 number of ANSYS BEAM189, and mesh size of $L^A/64$ ABAQUS SOLID C3D8 are used.

5.3. Bending problem - internal contact

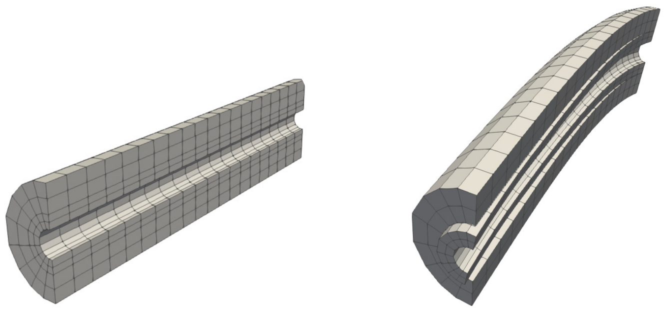

(a) Initial configuration (b) Deformed configuration

Figure 15: Interconnected beams using discretization of four beam elements

This example examines the introduced surface-to-surface contact formulation when the internal contact description is considered. Two interconnected beams with the C-shape cross-sections, undergo a large global deformation due to an applied nodal force at the outer beam's end-point. The geometrical and material parameters used in this example are identical to those in 5.2 except for $H^A = H^B/2$ and $W^A = W^B/2$. An external nodal force of $f_y = -3.5 \cdot 10^8 (H^B)^3$ N is applied at the outer beam's end. Figures 15a and 15b respectively show the interconnected beam structure at the beginning and the end of simulation. As is evident from Figure 15b, as well as the global bending deformation, a lateral warping occurred due to the torsional moment induced by the unsymmetrical distribution of the applied force over the cross-section plane. As a consequence of such loading induction, the inner beam rotated in the direction opposite to the outer C-shape cylinder within the contact. Figure 16 plots the trajectory of the middle contact line of the structure based on the solutions obtained by the proposed formulation in Section 4 and the quadratic solid element type in ABAQUS. The figure indicates an acceptable agreement between the two solutions for this complex contact scenario. The extrema values for the end-point of the outer beam are collected in Table 3. The table shows that the lateral deformation in the z direction, mainly emanating from the induced lateral warping and bending, was captured by the developed surface-to-surface contact formulation with the ANCF beam

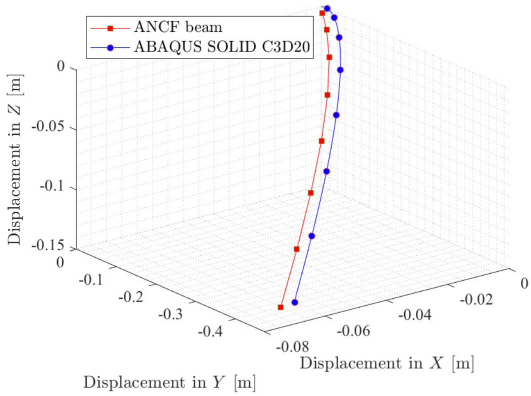

Figure 16: Comparison between the solutions for the outer beam centre line position field using the proposed contact formulation and ABAQUS. Discretizations of eight ANCF beams, and mesh size of 0.025 with SOLID C3D20 are used.

Table 3
Displacement of the end-point of the outer beam based on the ANCF solution according to the surface-to-surface contact formulation and that obtained using ABAQUS solid C3D20

Solution [element size]	Disp. in x [m]	Disp. in y [m]	Disp. in z [m]
ANCF [$L/4$]	-0.07473	-0.46637	-0.13273
ABAQUS [$0.025A_cL$*]	-0.06770	-0.45438	-0.13754

$*A_c = \pi\left((\frac{W^A}{2})^2 - (\frac{W^B}{2})^2\right)/2$

535 and is in excellent agreement with the solid element in ABAQUS. The vertical and axial displacements given by
536 the introduced approach are also in acceptable agreement with the ABAQUS solution. Such a small difference in
537 vertical displacement solutions between the ANCF and ABAQUS solid element is predictable for the ANCF beam element with linear interpolation in the cross-sectional directions, see [43, 62] for detailed discussions. Fig 17

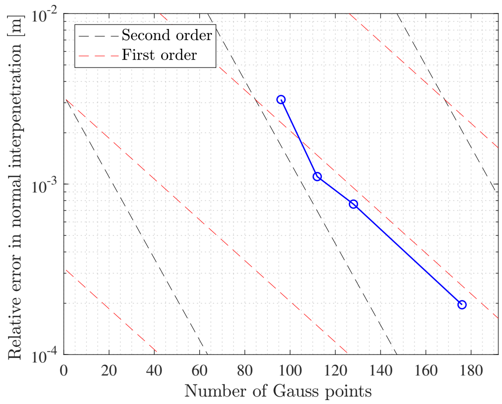

Figure 17: Rate of mitigation of interpenetration as a function of the Gauss points used when beam discretization of four elements is applied in the case of the internally contacting beams undergoing bending. Red and black dashed lines respectively represent the first and second order of convergence rates.

538
539 shows that the relative error of interpenetration starts to diminish at a second-order pace and by the further increas-

ing of the Gauss points across the contacting surfaces, it continues at a first-order rate. The relative error approaches to its minimum value in the quadratic order from the second data point where $n_{GT} > 120$. Figure 18 provides a

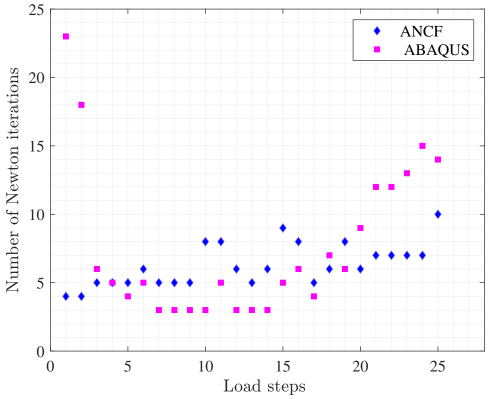

Figure 18: Number of iterations required to achieve a converged solution according to the stopping criterion (16) using our in-house code at each load step in comparison with the number of iterations required in ABAQUS to solve the internal contact problem of beams under bending.

comparison between the required number of Newton's iterations to achieve a converged solution for the global system of equations using the proposed contact formulation (according to criterion (16)) and ABAQUS. Overall, the solution given by the proposed formulation obtained with a less computational effort in terms of required number iterations.

5.4. Axial internal contact problem

This example illustrates the internal contact between the interconnected beams ($g_0 = 0$) with the cross-section properties which are identical to those in the previous subsection. The internal contact pressure between the inner and outer beams is to be applied by imposing the unixial force $f_y = -10^9 \cdot H^3$ on the inner beam's free end. The geometrical parameters of this example are identical to those in 5.3, $E = 2.07 \cdot 10^9$ and $\nu = 0.3$.

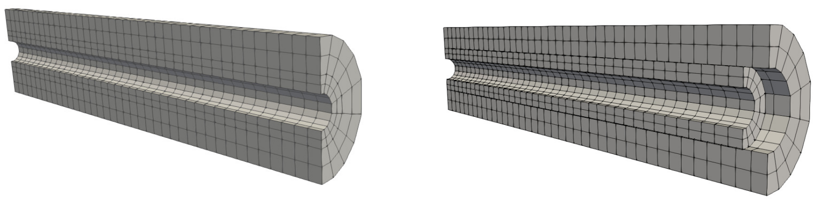

(a) Initial configuration (b) Deformed configuration

Figure 19: IntInterconnected beams under an unixial load applied on the inner beam. The result is based on eight ANCF beam discretization.

Figures 19a and 19b visualizes the solution of the interconnected C-shape cylinders at the beginning and end of simulation, respectively.

Figure 20 shows the rate of convergence in terms of the interpenetration between the interconnected beams. It indicates that by increasing the number of Gauss points (ascending number of integration segments), the gap distance converged well to a small value. To investigate the accuracy of the converged solutions for the axial displacement of the inner beam and the radial displacement of the outer beam, a comparison against the corresponding solutions

Table 4
Comparison of the axial and radial displacements of the inner and outer beams, respectively obtained by the proposed contact formulation against ABAQUS

Solution [element size]	Inner beam axial disp. [m]	Outer beam radial disp. [m]	Interpenetration [m]
ANCF [$L/8$]	-0.07744	0.002746	-1.48937×10^{-5}
ABAQUS [$0.025A_cL$*]	-0.07689	0.002425	-3.18285×10^{-4}

*$A_c = \pi\big((\frac{W^A}{2})^2 - (\frac{W^B}{2})^2\big)/2$

557 given by commercial finite element code ABAQUS was made. The displacement results are collected in Table 4. The
558 results are based on the eight discretizations used with the ANCF and the mesh size of 0.025 m with the solid 20-node
559 element using ABAQUS. The results given by the internal surface-to-surface formulation with the ANCF beam are
560 in acceptable agreement with those acquired by ABAQUS. The gap distance value in the case of the ANCF element
561 solution is significantly smaller than that given by the solid element in ABAQUS. It is also in compliance with
562 Figure 20 which shows that the interpenetration decreases with increase of the number of integration points across
563 the contacting surfaces. Whereas in the case of the lowest number of Gauss points, the gap distance is close to the
564 value reported from ABAQUS. It indicates that the surface segmentation considerably reduces the interpenetration,
565 and consequently, provides a converged solution using a reasonable number of beam discretizations.

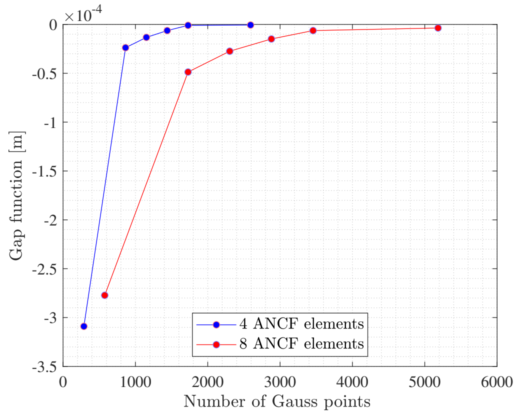

Figure 20: Interpenetration as a function of the Gauss points used when beam discretizations of four and eight elements are used for the axial internal contact problem.

566 ## 5.5. Twisting beams contact problem

567 This sub-section considers the pure twisting of two parallel beams. Three cross-sectional shapes are considered
568 in this section. First, two contacting beams of rectangular cross-section shape undergo a torsional moment. Sec-
569 ond, the beams with an elliptical cross-section are investigated and third, beams with honeycomb cross-section are
570 examined.

571 ### *5.5.1. Rectangular cross-section*

572 In the case of beams with rectangular cross-section, a maximum nodal torque of m_x is applied at both beam ends,
573 see Table 5. The two beams are clamped on one end. In this example, both the Saint Venant-Kirchhoff and Neo-
574 Hookean material models are used. Figure 21 shows the initial and deformed configurations of the structure with
575 increasing value of torsional moment m_x, expressed in terms of the angle of twist $\theta \in [0.5\pi, 0.625\pi, 0.7\pi, 0.75\pi]$
576 rad. It can be realised from the figure that at $\theta = 0.7\pi$ there is sharp edge-to-sharp edge contact including the

Table 5
Parameters of twisting beams problem with a rectangular cross-section

Parameters	Value*
Young's modulus E [Pa]	$2.07 \cdot 10^{11}$
Poisson ratio ν	0.3
Shear modulus μ [Pa]	$\mu = E/\big(2(1+\nu)\big)$
Maximum applied torque m_x [N.m]	$0.75\pi\mu J_t/L$
$L = L^A = L^B$ [m]	4
$H^A = H^B$ [m]	0.2
$W^A = W^B$ [m]	0.4

* $J_t = \beta W H^3$ where $\beta = 0.229$

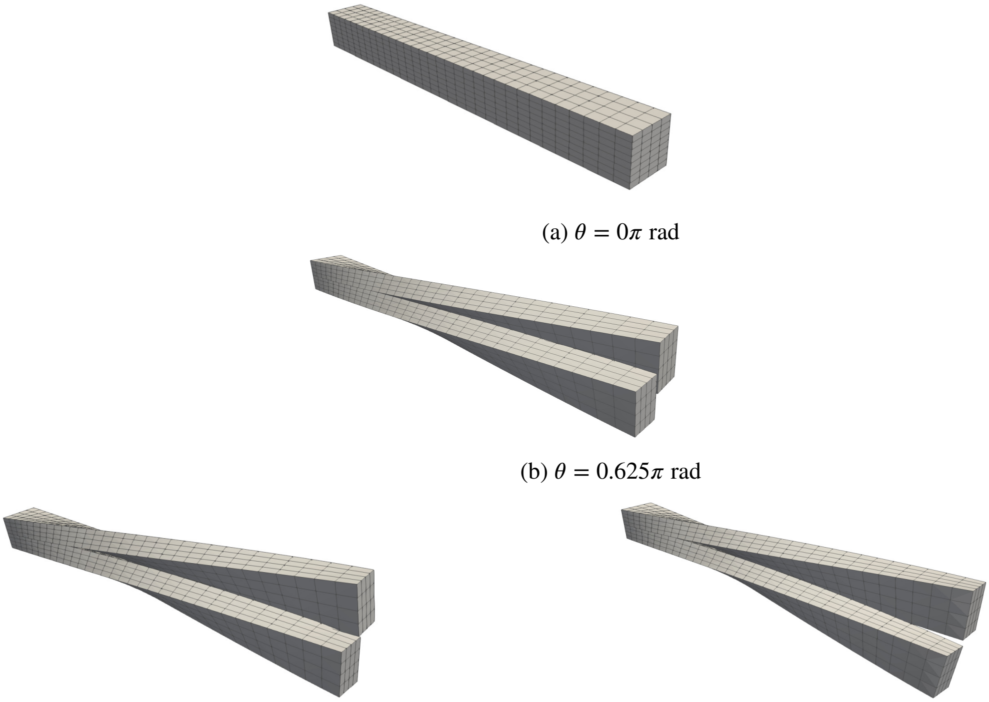

(a) $\theta = 0\pi$ rad

(b) $\theta = 0.625\pi$ rad

(c) $\theta = 0.7\pi$ rad

(d) $\theta = 0.75\pi$ rad

Figure 21: Deformed configurations of the twisted structure with a rectangular cross-section with increasing values of angle of twist θ. The results are based on the discretization of eight ANCF elements. The grey grids denote the imported solid-based mesh of a unit volume of an undeformed structure to be spatially visualised in the post-processing using Paraview.

beam's cross-section corners. So, this sharp edge contact can be interpreted as a specific state of the surface-to-surface contact. Figure 22 compares rate of convergence of the interpenetration mitigation in terms of the number of Gauss points used in the computation of variation of the strain energy for both the material models employed. One can notice a converged value for the interpretations within a certain number of Gauss points with both the materials used. The Saint Venant-Kirchhoff material converged to a smaller value for the gap distance ($g_N = -3.2011 \cdot 10^{-4}$) compared to that of the Neo-Hookean material ($g_N = -1.2306 \cdot 10^{-3}$).

Figure 23 plots the relative error of the norm of contact forces (reaction force) exerted from the entire slave

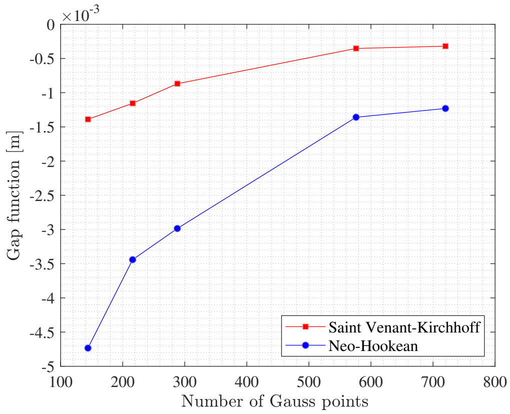

Figure 22: Interpenetration as a function of the Gauss points used when beam discretization of four ANCF beams is used with the Saint Venant-Kirchhoff and Neo-Hookean material models. The beams' cross-section is of rectangular shape.

beam A in the case of the Saint Venant-Kirchhoff and Neo-Hookean materials in terms of the ascending number of degrees-of-freedom. One can realize from the figure, that both material models exhibit a converged solution for the induced contact reaction force, while the values resulted from the material models employed disagree. This indicate the different values of norms for the contact force vectors obtained with both the material models employed. This was expected when recalling Figure 22 that indicates the larger values of interpenetration with the Neo-Hookean solution compared with the interpenetration values reported by the Saint Venant-Kirchhoff material model. This discrepancy is relevant to the smaller value of the penalty parameter having to be used with the Neo-Hookean material model ($p_n = 10^7$) than that which was selected with the Saint Venant-Kirchhoff material model ($p_n = 10^8$).

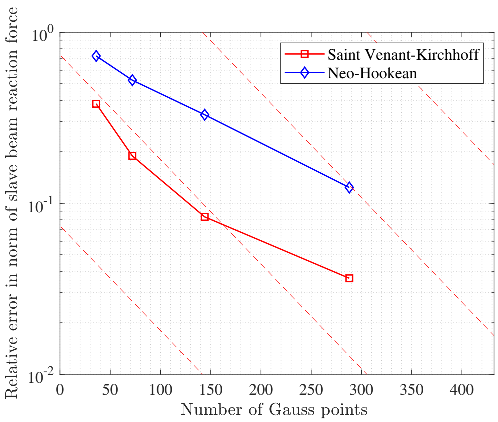

Figure 23: Relative error of norm of the vector of contact forces $\left\|\boldsymbol{F}^A_{\text{con}}\right\|$ exerted from the entire slave beam with increasing number of beam discretizations when the Saint Venant-Kirchhoff and Neo-Hookean material models are used. A rectangular cross-section is used in the structure. The dashed red lines denote the first order of convergence rate.

5.5.2. Elliptical cross-section

In this example, the previous twisting beam contact problem is considered with an elliptical cross-section. Again, the structure is clamped at one of its ends. All of the simulation parameters except for the cross-sectional parameters, are identical to those in Table 5. The cross-sectional properties are $H^A = H^B$ m and $W^A = W^B$ m. The maximum applied torque is $m_x = \pi\mu J_t/L$ N.m where $J_t = \dfrac{\pi W^3 H^3}{W^2 + H^2}$.

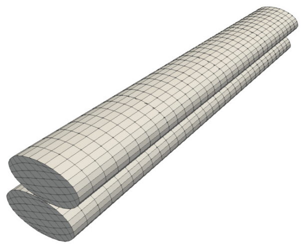

(a) $m_x = 0$ N.m

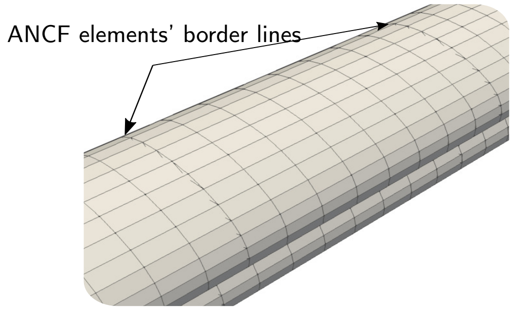

(b) ANCF elements' border is designated by small oblique lines.

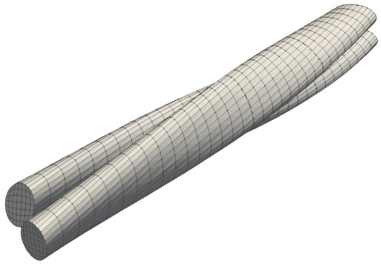

(c) $m_x = \dfrac{0.05\pi\mu J_t}{L}$ N.m

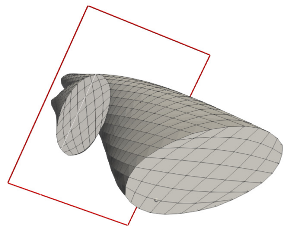

(d) Clipped slave beam shown in (c)

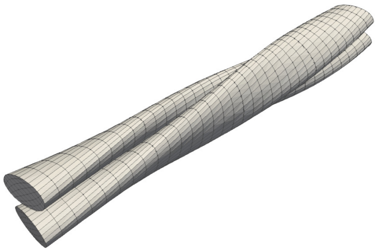

(e) $m_x = \dfrac{0.0625\pi\mu J_t}{L}$ N.m

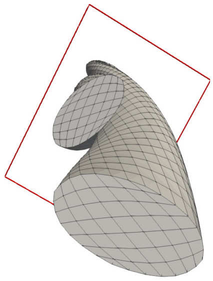

(f) Clipped slave beam shown in (e)

Figure 24: Deformed configurations of the twisted structure with an elliptical cross-section with increasing values of angle of twist θ. The results are based on the discretization of four ANCF elements.

Figure 24 illustrates the initial and deformed configurations of the structure with increasing values of torsional moment m_x specified at the selected load steps in the figure. As evidenced by the figure, the structure's free end almost underwent a torsion angle of 180°. The cross-section deformation can be recognized from Figures 24e and 24f where the line-to-line contact evolved to the surface-to-surface. Figure 25 compares the interpenetration evolution with ascending number of Gauss points used in the computation of the variation of the strain energy for both the material models employed. The interpenetration corresponding to the Saint Venant-Kirchhoff material model converged to a value of ($g_N = -6.6876 \cdot 10^{-5}$) with a relatively lesser number of Gauss points used to parametrize the contact patch, compared to that of the Neo-Hookean material ($g_N = -2.1339 \cdot 10^{-4}$).

Figure 26 displays the relative error of the norm of contact forces, exerted from the entire slave beam A for both the Saint Venant-Kirchhoff and Neo-Hookean material models in terms of the ascending number of degrees-

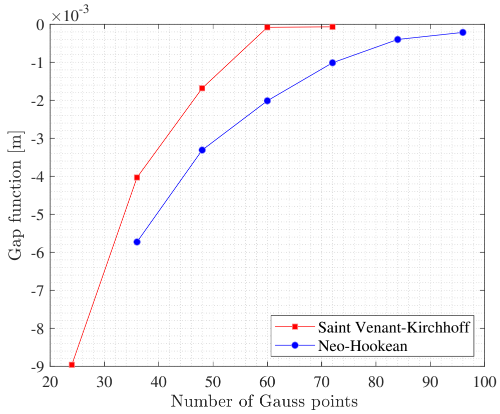

Figure 25: Interpenetration as a function of the Gauss points used when beam discretization of four ANCF beams is used with the Saint Venant-Kirchhoff and Neo-Hookean material models. The torsion of $m_x = \dfrac{0.025\pi\mu J_t}{L}$ N.m with a single load step is applied.

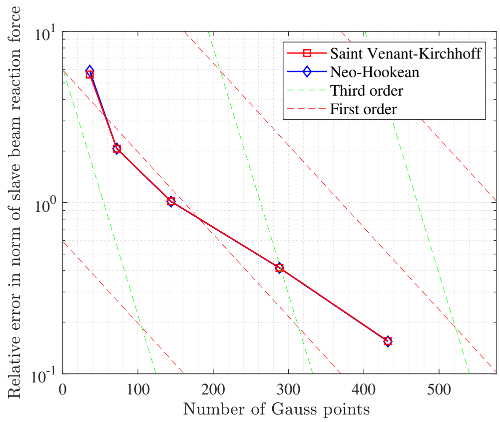

Figure 26: Relative error of norm of the vector of contact forces exerted from the entire slave beam with increasing number of beam discretizations when the Saint Venant-Kirchhoff and Neo-Hookean material models are used.

of-freedom. Solutions for both the material models exhibit an acceptable convergence rate for the induced contact reaction force with a reasonable beam discretization (moderately course mesh). Moreover, it is interpreted from the figure that, the values of the norm of contact forces in the case of both material models agree well. It was expected as a result of using a certain value of $p_n = \mu J_t$ for the penalty parameter in both material models. While different descriptions for the strain energy functions were used for the Neo-Hookean material model with the deformation gradient-based internal energy potential, and the Saint Venant-Kirchhoff model with the strain-based internal energy function, they achieved the converged solutions with an acceptable agreement. Figure 27 shows the contact action-reaction in terms of the norm of contact forces imposed from the slave and master beams. The torsional load was prescribed with respect to an exponentially increasing function

$$m_x^i = \Big(\frac{0.0625\pi\mu J_t}{L}\Big)(1 - e^{-\frac{10i}{n_{ls}}}) \quad \text{with} \quad i = 1, ..., n_{ls}, \tag{64}$$

where n_{ls} is the maximum number of load increments. The almost balanced norm of vector of contact forces associated with the slave and master beams illustrated in Figure 27, concretely implies that the weak form of contact energy potentials were unbiasedly integrated over both the master's and slave's surfaces. This can be compared with the unbiased treatment of weak form of the contact potential over the two contacting surfaces in virtue of introducing the two-half-pass algorithm in [22]. The figure shows that the contact force magnitudes were evaluated almost smoothly by increasing the torsional load applied. Figure 28 compares the required number of iteration attempts to achieve a converged solution at each load increment in the case of both material models. According to the figure, when using the Neo-Hookean material, the least number of iterations were needed. In can be explained by recalling that the prescribed torsion is a function of twist angle, see Eq. (64), and the stress-strain relation in the case of Neo-Hookean material model can be approximated with respect to an exponential function.

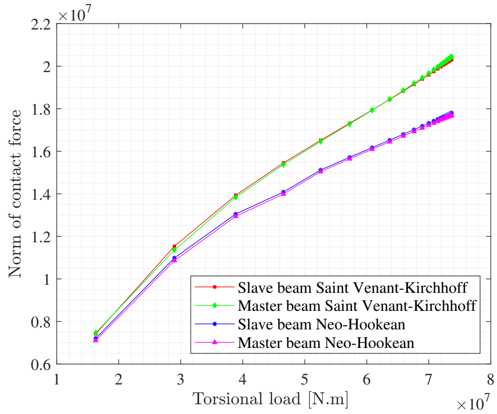

Figure 27: Evolution of norm of the vectors of contact forces exerted from the master and slave beams denoted $\left\|\boldsymbol{F}^{B}_{\text{con}}\right\|$ and $\left\|\boldsymbol{F}^{A}_{\text{con}}\right\|$, respectively evaluated at each load step using the Saint Venant-Kirchhoff and Neo-Hookean material models.

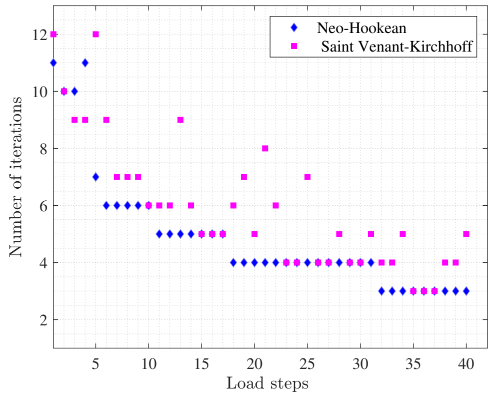

Figure 28: Number of iterations required to achieve a converged solution according to the stopping criterion (16) when solving the global system of equations at each load step for the twisting beams with the elliptical cross-section.

5.5.3. Honeycomb cross-section

The final example focuses on the usability of the proposed contact formulation in the case of a highly sophisticated cross-section. The honeycomb shape beam consists of a central elliptical core surrounding by six elliptical petals which are mutually connected to the central ellipse. Two geometrically identical beams with the length of $L = 5$ m, the lateral dimensions of $W = 0.6$ m and $H = 0.539595$ m are wrapping around each others as shown in Figure 29. The polar moment of inertia for the honeycomb cross-section is given as $J_t = 0.39575$ m^4. The material properties of the beams are identical to the previous example in Section 5.5.2. The maximum torsional load of $m_x = \dfrac{0.020\pi\mu J_t}{L}$ N.m and an axial tensile load of $f_x = 3.75 m_x$ N are gradually applied according to a quadratic function within 40 load steps on the structure's free end. The deformed shape of the structure at the end of the loading is shown in Figure 30a. Figure 30b illustrates the contacting beams cross-section when the structure is clipped at $x \approx \dfrac{3}{4}L$. Figure 31 compares the norm of the vectors of contact force exerting from the master and slave beams when both the beams are discretized using four elements and one segment is used to discretize the contacting surfaces. The norm of actions-reaction forces are almost identical within the most of the load steps, that indicates the unbiasedly integration of the contact energy on both the contacting surfaces.

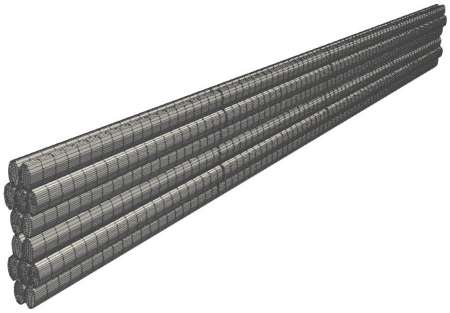

Figure 29: Initial configuration of two structures with honeycomb cross-section

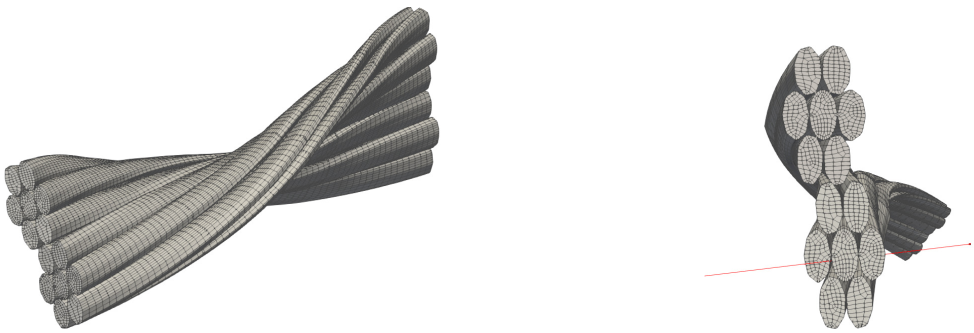

(a) $m_x = \dfrac{0.017\pi\mu J_t}{L}$ N.m, $f_x = 3.75 m_x$ N

(b) Clipped structure shown in (a)

Figure 30: Deformed configuration of the twisted structure with a honeycomb-shape cross-section at the end of simulation based on the discretization of four ANCF elements.

In the case of contact between beams with different orientations, the only further task is the identifying of the region of contact in terms of the elements and segments involved. This task can properly be carried out by identifying the close-by elements using, for example, the broad phase search for contacting elements such as what has been used in [47].

6. Conclusions

A novel approach for the description of contact in the case of slender continua with arbitrary cross-sectional geometry was introduced within this paper. The introduced approach was formulated in the framework of the absolute nodal coordinate formulation. The numerical results indicate that the proposed approach is sufficiently robust,

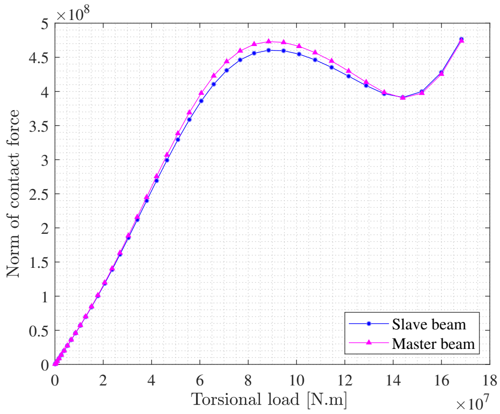

Figure 31: Evolution of the norm of the vectors of contact forces exerted from the master and slave beams denoted $\left\|\boldsymbol{F}^B_{\text{con}}\right\|$ and $\left\|\boldsymbol{F}^A_{\text{con}}\right\|$, respectively evaluated at each load step. The solution is based on the Neo-Hookean material model and using four beam elements.

accurate, and applicable in the problems in which the beam-like structures with non-trivial cross-section shape come into contact such as soft, slender biological tissues. The contact path test delivered the acceptable results that showed the performance of the proposed surface-surface integration scheme. The inf-sup condition was satisfied that indicates the stability of the formulation. Moreover, owing to the fully interpolated beam's surface with the proposed contact formulation, an arbitrary curve-to-curve contact, e.g. contact between spiral patches in beams with non-conformal cross sections that wrap around each other can be described. With the twisting beam problems, the unbiased treatment of the arbitrary contact patch was observed. Utilizing the Gauss points in the interpolated beam's cross-section in the material description, averts a step of computational effort for a further parameterization of the contacting surface in terms of the spatial points in the transverse directions. The introduced contact description can be utilized with beams with non-typical cross-sections where a contact region is relatively large enough to be regarded as surface-to-surface contact or on the contrary, is sufficiently small enough to be considered as the point-based or the line-based contact, e.g., contact involving sharp edges. In our forthcoming contribution, the presented contact description will be adopted to solve contact problems between several pre-twisted biological tissues with geometrically inhomogeneous cross-sections.

Acknowledgements

This research was partially supported by the Academy of Finland within the application number 299033 and Flanders Innovation & Entrepreneurship Agency within the COMPAS project. Also, the KU Leuven research fund is gratefully acknowledged.

A. Appendix

Algorithm 1 Surface-to-surface integration schemes for the external and internal contact descriptions

loop over the slave beam to check distance between the both master end-points and the slave elements (search for the closest slave element ID to the master end-points)
for i = $1 : n^A$ **do**
end for ⊳ closest slave element number (ID) to master 1^{st} and 2^{nd} master end-points were identified.
The recorded vector of nodal coordinates corresponds to the closest slave element are retrieved on which the master end-points are projected using Eq.(33). ⊳ The left boundary of the first slave integration segment $\xi^A_{s,1_e}$ is identified ⊳ The right boundary of the last slave integration segment $\xi^A_{s,2_e}$ is identified
for i = $n^{(1e)} : n^{(2e)}$ **do** ⊳ Loop over the slave contacting elements
    for j = $1 : n^j_G$ **do** ⊳ Loop over the slave Gauss points
        for k = $1 : n_S$ **do** ⊳ Loop over the slave segments
            Equidistantly slave element segmentation if no projection for the master end-point exists
            Calculation of the Gauss points and their weights on the slave beam ⊳ The vector of the abscissa coordinate parameter ξ^A_{sj}) on entire contacting elements on slave beam after segmentation is recovered
        end for
    end for
end for⊳ The Gauss points on the slave beam are to be projected back to the master beam through the following procedure
for i = $1 : n^B$ **do** ⊳ Loop over the master beam to assign the slave Gauss point to the closest master beam
    for i = $n^{(1e)} : n^{(2e)}$ **do** ⊳ Loop over the slave contacting elements
        for k = $1 : n_{GT}$ **do** ⊳ Loop over the total Gauss points along the slave beam centre line
            Position vector field of Gauss points on the slave surface is recorded
        end for
    end for
end for
for k = $1 : n_{GT}$ **do** ⊳ Loop over the total Gauss points along the slave beam centre line
    for i = $1 : n^B$ **do**
        Find the closest master element to each Gauss point on the slave beam
    end for
end for
An element ID, where the Gauss points belong to, is recorded for the all Gauss points on the slave beam
for k = $1 : n_{GT}$ **do**
    Get the Gauss coordinate parameter $\xi^B(\xi^A_{sj})$ on the master beam after projecting them
end for ⊳ The full set of the Gauss coordinate parameters on the master beam are saved into a vector
An element ID, where the projected Gauss points belong to, is recorded for the all Gauss points on the Slave beam ⊳ The following procedure establishes surface segmentation in the case of an external or an internal contact
if There is an external contact **then**
    Recovering the Gauss points on the external cross-section portion of the master beam where an active contact exists
    The Gauss points values in η and ζ direction and their weights are recovered in to three separate vectors
end if
if There is an internal contact **then**
    Recovering the Gauss points on the internal cross-section portion of the slave beam (in the case of hollow-type cross-sections) where an active contact exists
    The Gauss points values in η and ζ direction and their weights are recovered in to three separate vectors
end if
for k = $1 : n^k_G$ **do** ⊳ Loop over the Gauss points on the beam cross-section portion where an active contact exists
    for k = $1 : n_{GT}$ **do** ⊳ Loop over the total Gauss points along the slave beam centre line
        Position vector field of Gauss points on an active contact surface of the on the master beam cross-section is recorded Solving the orthogonality problems for η^B and ζ^B to project the Gauss points on the master beam contact surface Solving the orthogonality problems for η^A and ζ^A to project the Gauss points on the slave beam contact surface
        Calculate the contact force contributions appeared in Eqs. (48) and (57) for the external and internal contact descriptions, respectively
    end for
end for

References

[1] J. C. Simo, P. Wriggers, R. L. Taylor, A perturbed lagrangian formulation for the finite element solution of contact problems, Computer Methods in Applied Mechanics and Engineering 50 (2) (1985) 163–180. doi:10.1016/0045-7825(85)90088-X.

[2] G. Zavarise, P. Wriggers, A segment-to-segment contact strategy, Mathematical and Computer Modelling 28 (4-8) (1998) 497–515. doi:10.1016/S0895-7177(98)00138-1.

[3] P. Wriggers, Computational Contact Mechanics, Springer-Verlag, Berlin, Heidelberg, 2006. doi:10.1007/978-3-211-77298-0.

[4] G. Haikal, K. D. Hjelmstad, A finite element formulation of non-smooth contact based on oriented volumes for quadrilateral and hexahedral elements, Computational Methods in applied mechanics and engineering 196 (2007) 4690–4711. doi:10.1016/j.cma.2007.06.002.

[5] D. del Pozo, I. Lopez-Gomez, I. Romero, A robust asymmetrical contact algorithm for explicit solid dynamics, Computational Mechanics 64 (1) (2018) 15–32. doi:10.1007/s00466-018-1654-x.

[6] P. Łitewka, Hermite polynomial smoothing in beam-to-beam frictional contact, Computational Mechanics 40 (5) (2006) 815–826. doi:10.1007/s00466-006-0143-9.

[7] N. El-Abbasi, K.-J. Bathe, Stability and patch test performance of contact discretizations and a new solution algorithm, Computers and Structures 79 (16) (2001) 1473–1486. doi:10.1016/S0045-7949(01)00048-7.

[8] D. Durville, Finite element simulation of textile materials at mesoscopic scale, in: Finite element modelling of textiles ans textile composites, Saint-Petersbourg, Russia, 2007, pp. 15–34. doi:10.1007/978-1-4020-6856-0_2.

[9] D. Durville, I. Baydoun, H. Moustacas, G. Périé, Y. Wielhorski, Determining the initial configuration and characterizing the mechanical properties of 3D angle-interlock fabrics using finite element simulation, International Journal of Solids and Structures 154 (2018) 97–103. doi:10.1016/j.ijsolstr.2017.06.026.

[10] C. Meier, A. Popp, W. A. Wall, A finite element approach for the line-to-line contact interaction of thin beams with arbitrary orientation, Computer Methods in Applied Mechanics and Engineering 308 (2016) 377–413. doi:10.1016/j.cma.2016.05.012.

[11] C. Meier, A. Popp, W. A. Wall, A unified approach for beam-to-beam contact, Computer Methods in Applied Mechanics and Engineering 315 (2017) 972–1010. doi:10.1016/j.cma.2016.11.028.

[12] C. Meier, A. Popp, W. A. Wall, A locking-free finite element formulation and reduced models for geometrically exact kirchhoff rods, Computer Methods in Applied Mechanics and Engineering 290 (2015) 314–341. doi:10.1016/j.cma.2015.02.029.

[13] R. A. Sauer, L. De Lorenzis, A computational contact formulation based on surface potentials, Computer Methods in Applied Mechanics and Engineering 253 (2013) 369–395. doi:10.1016/j.cma.2012.09.002.

[14] M. A. Puso, T. Laursen, A mortar segment-to-segment frictional contact method for large deformations, Computer Methods in Applied Mechanics and Engineering 193 (2004) 4891–4913. doi:10.1016/j.cma.2004.06.001.

[15] A. G. Neto, P. Wriggers, Computing pointwise contact between bodies: a class of formulations based on master–master approach, Computational Mechanics 64 (3) (2019) 585–609. doi:10.1007/s00466-019-01680-9.

[16] A. G. Neto, P. Wriggers, Numerical method for solution of pointwise contact between surfaces, Computer Methods in Applied Mechanics and Engineering 365 (2020) 112971. doi:10.1016/j.cma.2020.112971.

[17] P. Wriggers, G. Zavarise, On contact between three-dimensional beams undergoing large deflections, Communications in Numerical Methods in Engineerings 13 (6) (1997) 429–438. doi:10.1002/(SICI)1099-0887(199706)13:6<429::AID-CNM70>3.0.CO;2-X.

[18] A. G. Neto, P. M. Pimenta, P. Wriggers, A master-surface to master-surface formulation for beam to beam contact. part I: Frictionless interaction, Computer Methods in Applied Mechanics and Engineering 303 (2016) 400–429. doi:10.1016/j.cma.2016.02.005.

[19] A. G. Neto, P. M. Pimenta, P. Wriggers, A master-surface to master-surface formulation for beam to beam contact. part II: Frictional interaction, Computer Methods in Applied Mechanics and Engineering 319 (2017) 146–174. doi:10.1016/j.cma.2017.01.038.

[20] A. G. Neto, P. Wriggers, Master-master frictional contact and applications for beam-shell interaction, Computational Mechanics 66 (2020) 1213–1235.

[21] G. Zavarise, P. Wriggers, Contact with friction between beams in 3D space, International Journal for Numerical Methods in Engineering 49 (8) (2000) 977–1006. doi:10.1002/1097-0207(20001120)49:8<977::AID-NME986>3.0.CO;2-C.

[22] M. Magliulo, J. Lengiewicz, A. Zilian, L. A. Beex, Non-localised contact between beams with circular and elliptical cross-sections, Computational Mechanics 65 (5) (2020) 1247–1266. doi:10.1007/s00466-020-01817-1.

[23] J. Simo, A finite strain beam formulation, the three-dimensional dynamic problem. Part I, Computer Methods in Applied Mechanics and Engineering 49 (1) (1985) 55–70. doi:10.1016/0045-7825(85)90050-7.

[24] J. C. Simo, L. Vu-Quoc, A geometrically-exact rod model incorporating shear and torsion-warping deformation, International Journal of Solids and Structures 27 (3) (1991) 371–393. doi:10.1016/0020-7683(91)90089-X.

[25] G. Jelenic, M. Crisfield, Geometrically exact 3D beam theory: implementation of a strain-invariant finite element for statics and dynamics, Computer Methods in Applied Mechanics and Engineering 171 (1-2) (1999) 141–171. doi:10.1016/S0045-7825(98)00249-7.

[26] I. Romero, F. Armero, An objective finite element approximation of the kinematics of geometrically exact rods and its use in the formulation of an energy–momentum conserving scheme in dynamics, International Journal for Numerical Methods in Engineering 54 (12) (2002) 1683–1716. doi:10.1002/nme.486.

[27] C. Meier, A. Popp, W. A. Wall, Geometrically exact finite element formulations for slender beams: Kirchhoff–love theory versus Simo–Reissner theory, Archives of Computational Methods in Engineering 26 (2019) 163–243. doi:10.1007/s11831-017-9232-5.

[28] C. Meier, M. J. Grill, W. A. Wall, A. Popp, Geometrically exact beam elements and smooth contact schemes for the modeling of fiber-based materials and structures, International Journal of Solids and Structures 154 (2017) 124–146. doi:10.1016/j.ijsolstr.2017.07.020.

[29] A. A. Shabana, Flexible multibody dynamics: Review of past and recent developments, Multibody system dynamics 1 (2) (1997) 189–222. doi:10.1023/A:1009773505418.

[30] A. A. Shabana, Definition of the slopes and the finite element absolute nodal coordinate formulation, Multibody System Dynamics 1 (3) (1997) 339–348. doi:10.1023/A:1009740800463.

[31] L. P. Obrezkov, M. K. Matikainen, A. B. Harish, A finite element for soft tissue deformation based on the absolute nodal coordinate formulation, Acta Mechanica 231 (2020) 1519–1538. doi:/10.1007/s00707-019-02607-4.

[32] L. Obrezkov, P. Eliasson, A. B. Harish, M. K. Matikainen, Usability of finite elements based on the absolute nodal coordinate formulation for deformation analysis of the achilles tendon, International Journal of Non-Linear Mechanics 129 (2021) 103662. doi:10.1016/j.ijnonlinmec.2020.103662.

[33] J. C. Simo, L. Vu-Quoc, A three-dimensional finite-strain rod model. part II: Computational aspects, Computer methods in applied mechanics and engineering 58 (1) (1986) 79–116. doi:10.1016/0045-7825(86)90079-4.

[34] K. Nachbagauer, P. Gruber, J. Gerstmayr, A 3D shear deformable finite element based on the absolute nodal coordinate formulation, in: J.-C. Samin, P. Fisette (Eds.), Multibody System Dynamics, Vol. 561 of Computational Methods in Applied Sciences, Springer, Dordrecht, Vienna, Austria, 2013. doi:10.1007/978-94-007-5404-1_4.

[35] K. Nachbagauer, A. Pechstein, H. Irschik, J. Gerstmayr, A new locking-free formulation for planar, shear deformable, linear and quadratic beam finite elements based on the absolute nodal coordinate formulation, Multibody System Dynamics 26 (3) (2011) 245–263. doi:10.1007/s11044-011-9249-8.

[36] I. E. Edri, D. Z. Yankelevsky, O. Rabinovitch, Continuous beam-type model for the static analysis of arching masonry walls, European Journal of Mechanics - A/Solids 91 (2022) 104387. doi:10.1016/j.euromechsol.2021.104387.

[37] G. He, K. Gao, J. Jiang, R. Liu, Q. Li, Shape optimization of a flexible beam with a local shape feature based on ANCF, Journal of Advanced Mechanical Design, Systems, and Manufacturing 13 (2019) JAMDSM0059.

[38] G. He, M. Patel, A. Shabana, Integration of localized surface geometry in fully parameterized ancf finite elements, Computer Methods in Applied Mechanics and Engineering 313 (2017) 966–985. doi:10.1016/j.cma.2016.10.016.

[39] L. P. Obrezkov, B. Bozorgmehri, T. Finni, M. K. Matikainen, Approximation of pre-twisted achilles sub-tendons with continuum-based beam elements, Applied Mathematical Modelling 112 (2022) 669–689. doi:10.1016/j.apm.2022.08.014.

[40] S. Nikula, M. K. Matikainen, B. Bozorgmehri, A. Mikkola, The usability and limitations of the various absolute nodal coordinate beam elements subjected to torsional and bi-moment loading, European Journal of Mechanics / A Solids Accepted (2022).

[41] A. G. Neto, P. de Mattos Pimenta, P. Wriggers, Contact between spheres and general surfaces, Computer Methods in Applied Mechanics and Engineering 328 (2018) 686 – 716. doi:10.1016/j.cma.2017.09.016.

[42] M. K. Matikainen, O. Dmitrochenko, A. Mikkola, Beam elements with trapezoidal cross section deformation modes based on the absolute nodal coordinate formulation, in: International Conference of Numerical Analysis and Applied Mathematics, Rhodes, Greece, 2010, pp. 1266–1270. doi:10.1063/1.3497930.

[43] H. Ebel, M. K. Matikainen, V.-V. Hurskainen, A. Mikkola, Higher-order beam elements based on the absolute nodal coordinate formulation for three-dimensional elasticity, Nonlinear Dynamics 88 (2) (2017) 1075–1091. doi:10.1007/s11071-016-3296-x.

[44] L. P. Obrezkov, A. Mikkola, M. K. Matikainen, Performance review of locking alleviation methods for continuum ANCF beam elements, Nonlinear Dynamics 109 (2022) 531–546. doi:10.1007/s11071-022-07518-z.

[45] X. Yu, M. K. Matikainen, A. B. Harish, A. Mikkola, Procedure for non-smooth contact for planar flexible beams with cone complementarity problem, Proceedings of the Institution of Mechanical Engineers Part K: Journal of Multibody Dynamics 235 (2) (2021) 179—-196. doi:10.1177/1464419320957450.

[46] B. Bozorgmehri, M. K. Matikainen, A. Mikkola, Development of line-to-line contact formulation for continuum beams, in: ASME 2021 International Design Engineering Technical Conferences and Computers and Information in Engineering Conference, Online, Virtual, 2021, p. V002T02A004. doi:10.1115/DETC2021-70450.

[47] B. Bozorgmehri, X. Yu, M. K. Matikainen, A. B. Harish, A. Mikkola, A study of contact methods in the application of large deformation dynamics in self-contact beam, Nonlinear Dynamics 103 (1) (2021) 581–616. doi:10.1007/s11071-020-05984-x.

[48] L. Peng, Z.-Q. Feng, P. Joli, J. hua Liu, Y. jing Zhou, Automatic contact detection between rope fibers, Computers & Structures 218 (2019) 82–93. doi:10.1016/j.compstruc.2019.03.010.

[49] K. Nachbagauer, P. Gruber, J. Gerstmayr, Structural and continuum mechanics approaches for a 3D shear deformable ANCF beam finite element: Application to static and linearized dynamic examples, Journal of Computational and Nonlinear Dynamics 8 (2) (2013) 021004. doi:10.1115/1.4006787.

[50] B. Bozorgmehri, Finite element formulations for nonlinear beam problems based on the absolute nodal coordinate formulation, Ph.D. thesis, School of Energy Systems, LUT University (2021).

[51] C. T. Gasser, R. W. Ogden, G. A. Holzapfel, Hyperelastic modelling of arterial layers with distributed collagen fibre orientations, Journal of the Royal Society Interface 3 (6) (2006) 15–35. doi:10.1098/rsif.2005.0073.

[52] A. G. Holzapfel, Nonlinear Solid Mechanics: A Continuum Approach for Engineering Science, John Wiley & Sons, Inc., 2000. doi:10.1023/A:1020843529530.

[53] E. Eich-Soellner, C. Führer, Numerical methods in multibody dynamics, Vol. 45, Springer, 1998. doi:10.1007/978-3-663-09828-7.

[54] V. B. Shim, W. Hansen, R. Newsham-West, L. Nuri, S. Obst, C. Pizzolato, D. G. Lloyd, R. S. Barrett, Influence of altered geometry and material properties on tissue stress distribution under load in tendinopathic Achilles tendons – a subject-specific finite element analysis, Journal of Biomechanics 82 (2019) 142–148. doi:10.1016/j.jbiomech.2018.10.027.

[55] A. Sommariva, M. Vianello, Gauss-Green cubature and moment computation over arbitrary geometries, Journal of Computational and Applied Mathematics 231 (2009) 886–896. doi:10.1016/j.cam.2009.05.014.

[56] J. Gerstmayr, M. K. Matikainen, A. Mikkola, A geometrically exact beam element based on the absolute nodal coordinate formulation, Multibody System Dynamics 20 (4) (2008) 359–384. doi:10.1007/s11044-008-9125-3.

[57] G. Zavarise, L. De Lorenzis, A modified node-to-segment algorithm passing the contact patch test, International Journal for Numerical Methods in Engineering 79 (4) (2009) 379–416. doi:10.1002/nme.2559.

[58] G. Zavarise, D. Boso, B. A. Schrefler, A contact formulation for electrical and mechanical resistance, in: Contact mechanics, Vol. 103 of Solid Mechanics and Its Applications, Springer, Dordrecht, 2002. doi:10.1007/978-94-017-1154-8_22.

[59] M. A. Puso, T. Laursen, A mortar segment-to-segment contact method for large deformations solid elements, Computer Methods in Applied Mechanics and Engineering 193 (2003) 601–629. doi:10.1016/j.cma.2003.10.010.

[60] M. A. Crisfield, Re-visiting the contact patch test, International Journal for Numerical Methods in Engineering 48 (3) (2000) 435–449. doi:10.1002/(SICI)1097-0207(20000530)48:3<435::AID-NME891>3.0.CO;2-V.

[61] D. Chapelle, K. J. Bathe, The inf-sup test, Computers and Structures 47 (4) (1993) 537–545. doi:10.1016/0045-7949(93)90340-J.

[62] B. Bozorgmehri, V.-V. Hurskainen, M. K. Matikainen, A. Mikkola, Dynamic analysis of rotating shafts using the absolute nodal coordinate formulation, Journal of Sound and Vibration 453 (2019) 214–236. doi:10.1016/j.jsv.2019.03.022.